npj | Systems Biology and Applications

www.nature.com/npjsba

ARTICLE OPEN

Logarithmic sensing in *Bacillus subtilis* aerotaxis

Filippo Menolascina[1,2], Roberto Rusconi[3,4], Vicente I Fernandez[3,4], Steven Smriga[3,4], Zahra Aminzare[5], Eduardo D Sontag[6] and Roman Stocker[3,4]

Aerotaxis, the directed migration along oxygen gradients, allows many microorganisms to locate favorable oxygen concentrations. Despite oxygen's fundamental role for life, even key aspects of aerotaxis remain poorly understood. In *Bacillus subtilis,* for example, there is conflicting evidence of whether migration occurs to the maximal oxygen concentration available or to an optimal intermediate one, and how aerotaxis can be maintained over a broad range of conditions. Using precisely controlled oxygen gradients in a microfluidic device, spanning the full spectrum of conditions from quasi-anoxic to oxic (60 n mol/l–1 m mol/l), we resolved *B. subtilis'* 'oxygen preference conundrum' by demonstrating consistent migration towards maximum oxygen concentrations ('monotonic aerotaxis'). Surprisingly, the strength of aerotaxis was largely unchanged over three decades in oxygen concentration (131 n mol/l–196 μ mol/l). We discovered that in this range *B. subtilis* responds to the logarithm of the oxygen concentration gradient, a rescaling strategy called 'log-sensing' that affords organisms high sensitivity over a wide range of conditions. In these experiments, high-throughput single-cell imaging yielded the best signal-to-noise ratio of any microbial taxis study to date, enabling the robust identification of the first mathematical model for aerotaxis among a broad class of alternative models. The model passed the stringent test of predicting the transient aerotactic response despite being developed on steady-state data, and quantitatively captures both monotonic aerotaxis and log-sensing. Taken together, these results shed new light on the oxygen-seeking capabilities of *B. subtilis* and provide a blueprint for the quantitative investigation of the many other forms of microbial taxis.

npj Systems Biology and Applications (2017) **3,** 16036; doi:10.1038/npjsba.2016.36; published online 19 January 2017

INTRODUCTION

Oxygen mediates the conversion of carbon sources to cellular energy and is the most common electron acceptor used in cellular respiration. In order to locate optimal oxygen conditions in their environment, several species of bacteria have evolved the ability to sense and migrate along oxygen gradients, a strategy called aerotaxis.[1] Aerotaxis is fundamental to many ecological processes. Within microbial mats at the sediment–water interface, the filamentous bacteria *Beggiatoa* use aerotaxis to glide along steep vertical oxygen gradients toward preferred micro-oxic depths.[2] The sulfur-reducing bacteria *Desulfovibrio* swim to accumulate in regions of specific, low oxygen concentration (~500 n mol/l or 0.04%), where conditions are thermodynamically favorable for anaerobic respiration.[3] An important phytopathogenic bacterium, *Ralstonia solanacearum*, uses aerotaxis to attack the roots of its plant hosts, including tomato and banana plants, causing their wilting and death.[4] *Escherichia coli,* a common inhabitant of the lower digestive tract of warm blooded animals, has been found to exploit aerotaxis to cross the mucosal layer protecting epithelial surface in the intestine and expedite its colonization.[5] More recently, *Caulobacter crescentus*, a monotrichous bacterium found in aquatic environments, has been observed to perform aerotaxis, adjusting its motility based on a dynamic rescaling of oxygen gradients.[6] Besides its role in energy harvesting, aerotaxis is involved in collective bacterial migrations, including bioconvection, where bacteria that swim up oxygen gradients accumulate and render water denser, causing convection and mixing.[7,8]

Aerotaxis was the first of all microbial taxis behaviors (i.e., directional migration responses to external stimuli) to be described, when in 1881 Theodor Engelmann observed bacteria moving towards the chloroplasts of algae in response to the oxygen produced by photosynthesis.[9] Despite its early discovery, however, our understanding of aerotaxis has remained rather poor and mostly qualitative. For example, even for the model bacterium *Bacillus subtilis* it has remained unclear whether cells seek an optimal, intermediate oxygen concentration (e.g., 200 μ mol/l or ~15%;[1,10] percentage values are based on oxygen saturation in water under laboratory conditions (temperature 25 °C and pressure 100 kPa)) or swim towards the highest oxygen concentration available (1.3 m mol/l or 100%),[11] a strategy with potentially detrimental physiological effects.[12] Beyond this 'oxygen preference conundrum', even the obligately aerobic nature of *B. subtilis*,[13] once believed to be a robust trait of this organism, has recently been put to question by results documenting its anaerobic growth.[14] This lack of understanding of concentration preferences in aerotaxis, in turn, prevents quantitative predictions of population dynamics in oxygen gradients.

Sensing mechanisms for aerotaxis fall in two categories. A first mechanism is based on the sensing of the intracellular energy status to determine the need for additional oxygen. This mechanism belongs to the class of energy-tactic behaviors,[1] is

[1]Institute for Bioengineering, School of Engineering, The University of Edinburgh, Scotland, UK; [2]SynthSys—Centre for Synthetic and Systems Biology, The University of Edinburgh, Scotland, UK; [3]Ralph M Parsons Laboratory, Department of Civil and Environmental Engineering, Massachusetts Institute of Technology, Cambridge, MA, USA; [4]Institute of Environmental Engineering, Department of Civil, Environmental and Geomatic Engineering, Zurich, Switzerland; [5]The Program in Applied and Computational Mathematics, Princeton, NJ, USA and [6]Department of Mathematics, Hill Center Rutgers, The State University of New Jersey, Piscataway, NJ, USA.
Correspondence: F Menolascina (filippo.menolascina@ed.ac.uk) or ED Sontag (eduardo.sontag@rutgers.edu) or R Stocker (romanstocker@ethz.ch)
Received 21 June 2016; revised 13 September 2016; accepted 5 October 2016

found in *E. coli*, *Azospirillum brasilense*, *Salmonella tiphymurium* and *Pseudomonas aeruginosa*, and has received considerable attention.[15,16] In *E. coli*, aerotaxis is mediated by the receptors *Aer* and *Tsr*. The former has recently been proposed to monitor the cell's metabolic state by gauging the activity of the electron transport system,[17] whereas *Tsr* has been speculated to sense the proton-motive force, a measure of the potential energy stored in the cell.[18] A second mechanism for aerotaxis is based on the sensing of extracellular oxygen via its direct binding to heme-containing receptors like *HemAT*. This mechanism, independent of metabolism and similar to classic chemotaxis,[19] is found for example in *B. subtilis* and *Halobacterium salinarum*, and has received limited attention to date.[6,19] For both forms of aerotaxis, there are no quantitative models of the cellular response to oxygen gradients.

Here we present a high-resolution experimental characterization of aerotaxis, focusing on the case of direct oxygen sensing in *B. subtilis*, a gram positive bacterium that is widespread in a broad range of environments.[12] The robustness of the data and the breadth of conditions examined allowed us to identify a quantitative population model for aerotaxis in *B. subtilis* and to resolve the oxygen preference conundrum for this bacterium by demonstrating that cells seek the highest oxygen concentration available under the full spectrum of conditions tested.

Traditional techniques to study aerotaxis have only enabled very limited quantification of this migration strategy. Observations of bacterial populations in capillaries, sealed at one end and exposed to a controlled oxygen concentration at the other end, revealed the formation of bacterial bands.[1] These bands have been interpreted as evidence for preferred oxygen concentrations by bacteria, yet conclusive interpretation and a quantitative analysis have remained difficult, because oxygen gradients are governed by both diffusion and respiration and thus poorly quantifiable with this approach. Oxygen measurements with microelectrodes[20] partially addressed this problem but have the drawback of being invasive, altering the distribution of both bacteria and oxygen. In contrast, initial applications of microfluidic devices to chemotaxis[21] and aerotaxis[6,16] have demonstrated the potential of this approach to control gradients for taxis studies, while simultaneously visualizing population responses.

Here we used a new microfluidic device and computer-controlled gas mixers to generate precise, linear oxygen concentration profiles over oxygen conditions ranging from anoxic to oxic, and we applied video microscopy and image analysis to accurately quantify the response of extremely large numbers of individual cell coordinates. We observed that *B. subtilis* always swims towards the highest available oxygen concentration and, notably, displays the same magnitude of aerotaxis over oxygen gradients (∇C) spanning three orders of magnitude when the relative gradient ($\nabla C/C$) is conserved, indicating this bacterium rescales its response to oxygen gradients via logarithmic sensing. We show that the vastly improved level of environmental control and data robustness of this approach over traditional ones permits the identification of a predictive mathematical model of aerotaxis in *B. subtilis* that captures logarithmic sensing and provides a blueprint for the quantitative study of other forms of microbial taxis.

RESULTS AND DISCUSSION

To study the aerotactic response of *B. subtilis* we exposed the bacteria to linear concentration profiles of oxygen across a microchannel and quantified the spatial distribution of cells along the width of the channel, $B(x)$, at steady state. We devised a new microfluidic device made of polydimethylsiloxane (PDMS) featuring three parallel channels sealed by glass slides on the top and bottom (Figure 1a). The central 'test' channel hosts the cells, whereas the flanking 'oxygen control' channels each carry a flow

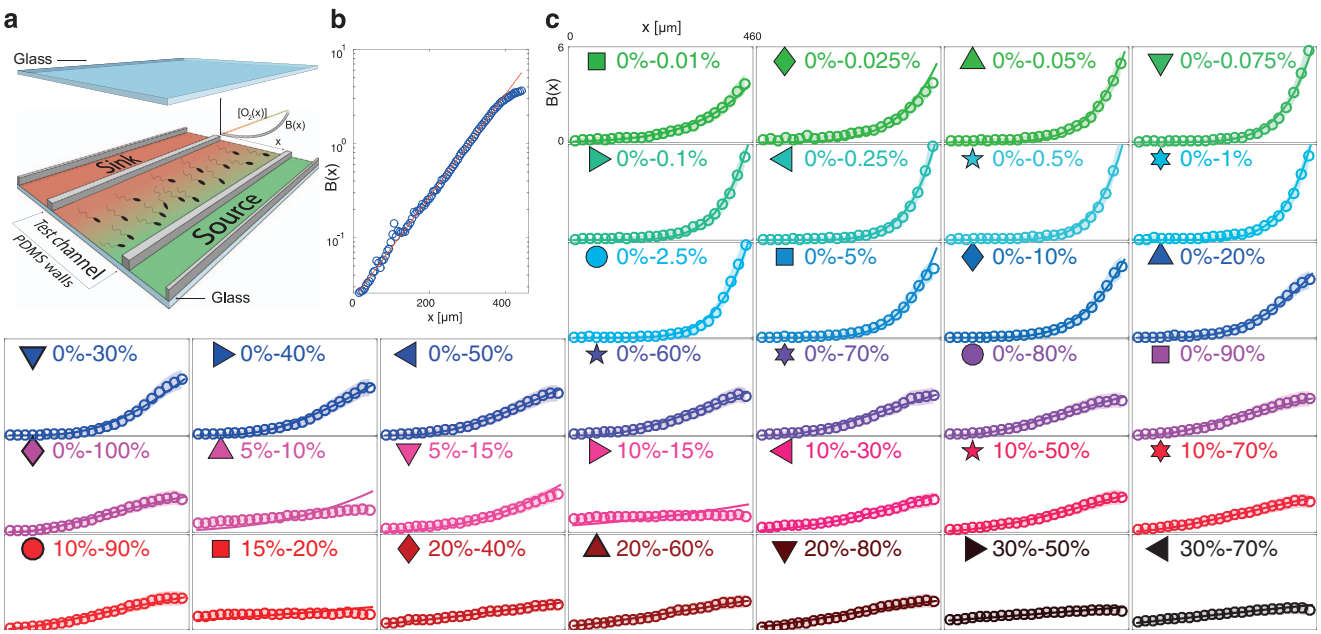

Figure 1. Aerotactic response of *Bacillus subtilis*. (**a**) The microfluidic device used to probe aerotaxis in *B. subtilis* consists of three parallel channels fabricated in polydimethylsiloxane (PDMS), with top and bottom glass surfaces. Flowing oxygen at prescribed concentrations in the source (green) and sink (red) channels created a linear oxygen concentration profile ($[O_2(x)]$) in the test channel, where the bacterial response was monitored by video microscopy. (**b**) Steady-state distribution of bacteria across the test channel, $B(x)$ (blue circles), for the 0–20% gradient (sink concentration—source concentration), along with the best exponential fit (red). (**c**) Steady-state aerotactic response, $B(x)$, for all 33 oxygen conditions tested. For each panel, the x axis represents the test channel width ($0 < x < 460$ μm) and the y axis represents $B(x)$ ($0 < B(x) < 6$). A uniform bacterial distribution would correspond to $B(x) = 1$. Open circles are experimental data, thin solid lines are model predictions, the shaded envelope represents plus/minus one standard deviation on the predictions. The oxygen concentrations in the sink and source channels are reported for each condition and a symbol is assigned to each condition for reference in subsequent figures.

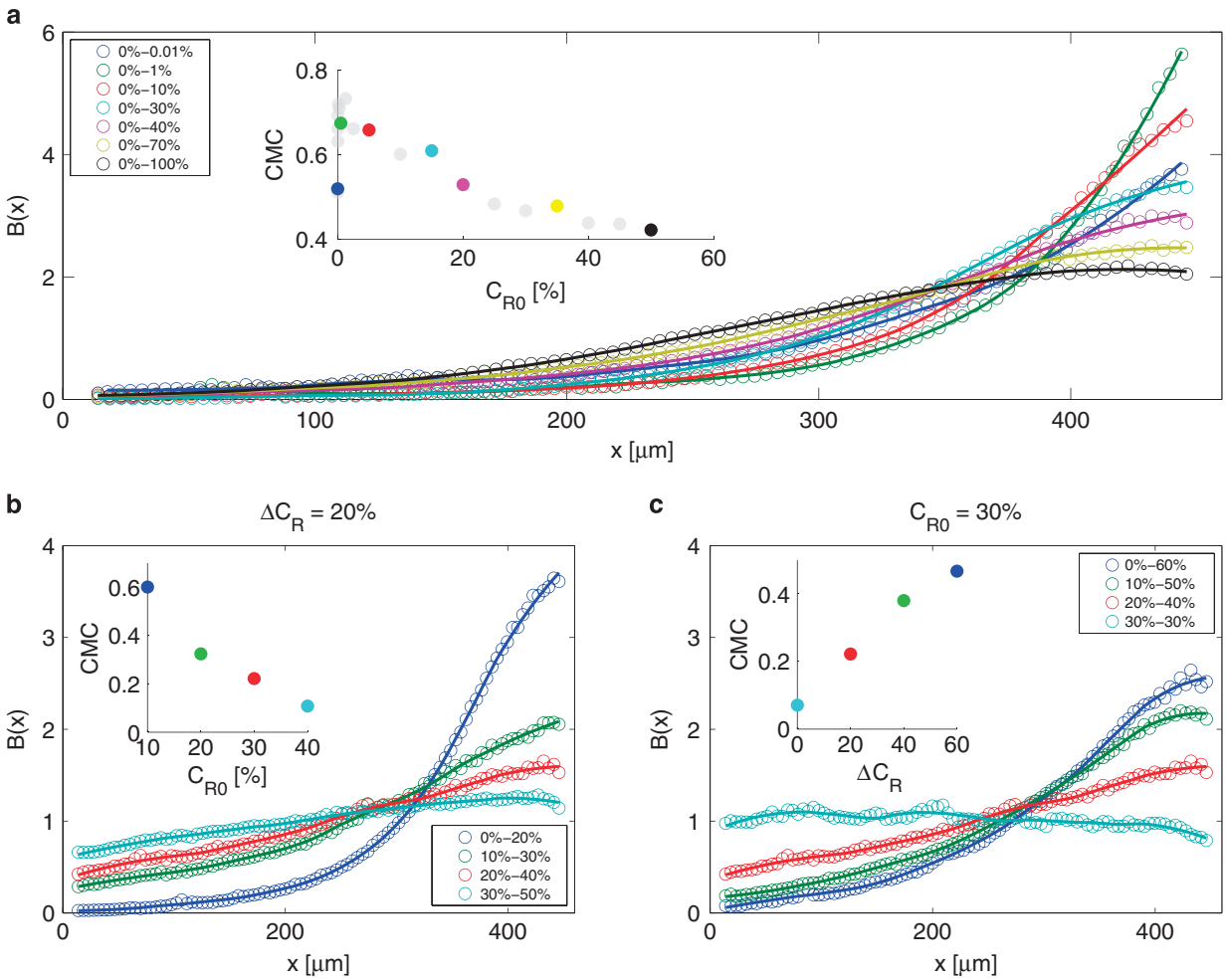

Figure 2. Oxygen preference in *B. subtilis* aerotaxis. (**a**) Normalized bacterial density profiles across the width of the test channel, $B(x)$, for a subset of the experiments of the form 0%–*X*% (sink concentration—source concentration). Open circles are experimental data, solid lines are a smoothed version of the same data obtained with a Savitzky–Golay filter. Inset: The Chemotactic Migration Coefficient (CMC) for the same experiments, as a function of the oxygen concentration C_{R0} at mid-channel ($x = 230$ µm). Color-coding of the data in the inset corresponds to the main panel, whereas gray circles are all other experiments of the form 0%–*X*%. (**b**) Aerotactic response, $B(x)$, in experiments in which the oxygen gradient was kept constant ($\Delta C_R = 20\%$ between source and sink channels) and the absolute oxygen concentration C_{R0} was varied. Inset: the CMC decreases with increasing absolute oxygen concentration. (**c**) Aerotactic response, $B(x)$, in experiments in which the oxygen gradient (i.e., ΔC_R) was varied and the absolute oxygen concentration C_{R0} was kept constant. Inset: the CMC increases with increasing oxygen gradient.

of oxygen at a prescribed concentration, higher in the 'source' channel and lower in the 'sink' channel (Figure 1a). Oxygen diffuses from the source channel to the sink channel through the PDMS (which is oxygen permeable[22]) and the test channel, where it thereby forms a gradient. The two glass slides, being impermeable to gas, force oxygen diffusion to occur only sideways, which leads to a linear oxygen profile. This provides less flexibility in setting up arbitrary gradients, compared with prior approaches,[16] but has the advantage of extreme fabrication simplicity (single-layer, two oxygen boundary conditions). A mathematical model of oxygen diffusion in this system (implemented in COMSOL Multiphysics 4.4; see 'Derivation and identification of the mathematical model' in Supplementary Materials and Methods), which also accounts for the top and bottom glass surfaces that are impermeable to oxygen, provides a quantitative prediction of the oxygen concentration and gradient that bacteria experience at every position in the test channel and confirms that the oxygen concentration profile is linear (Supplementary Figure S1). The model also shows that cells in the device are exposed to $>90\%$ of the total oxygen gradient between sink and source channels (see 'Oxygen diffusion within the device' and Supplementary Table S1).

To quantify aerotaxis we probed *B. subtilis*' response at steady state in 33 different gradients, spanning four decades in gradient magnitude (from 0.26 n mol/l/µm to 2.56 µ mol/l/µm) and ranging from 0%–0.01% to 0%–100%. Experiments therefore covered a large spectrum of the oxygen conditions that *B. subtilis* may experience in nature, from quasi-anoxic to fully oxygenated.

For all conditions tested, *B. subtilis* moved towards the highest oxygen concentration available (Figure 1c). Accumulation profiles $B(x)$ were mostly exponentially shaped (Figure 1b). Positive aerotaxis was observed even when the highest oxygen concentration in the test channel was near saturation (0%–100% gradient, Figure 1c). In contrast to previous reports of a preferred oxygen concentration of 200 µ mol/l (i.e., ~15%) for *B. subtilis*,[10] we consistently (19 experiments, Figure 1c) observed accumulation of cells to higher concentrations than 200 µ mol/l (although we did observe a decrease in the accumulation strength for oxygen concentrations above 20%; Figure 2a). These findings resolve the oxygen preference conundrum in *B. subtilis* and

demonstrate that these bacteria always swim towards the highest available oxygen concentration.

Aerotaxis was strongest at very low oxygen concentrations, in particular in the micromolar regime (Figure 1c). For example, the concentration of bacteria reached a value six-fold higher than the mean near the top of the 0%–1% (0–13 μ mol/l) gradient (Figure 2a). To assess the strength of accumulation of bacteria, we calculated the Chemotactic Migration Coefficient (CMC), a metric frequently used in the chemotaxis literature[21] that quantifies the distance that cells travel from the middle of the channel towards high chemoattractant concentrations (Figure 2a, inset). Focusing on gradients with 0% oxygen in the sink channel (Figure 2a), the strength of accumulation (CMC) showed a non-monotonic dependence on the mean oxygen concentration, C_{R0} (equivalently, the oxygen concentration at mid-channel, $x = 230$ μm). The CMC increased with C_{R0} for gradients going from 0%–0.01% (0.015%/mm) to 0%–1% (1.5%/mm) and decreased for gradients larger than 0%–1% (Figure 2a, inset).

The magnitude of the aerotactic response depended on both the strength of the gradient, ∇C ($= \Delta C_R/W$, where ΔC_R is the difference between source and sink concentrations and W is the width of the channel), and the mean concentration of oxygen in the test channel, C_{R0} (Figure 1c). To tease apart the contribution of these two factors, we carried out two sets of experiments. In the first set, the oxygen gradient was fixed ($\Delta C_R = 20\%$) and we varied the mean oxygen concentration ($C_{R0} = 10\%$ to 40%). These experiments indicate that the strength of accumulation, CMC, decreases with increasing mean concentration (Figure 2b). In the second set of experiments, the mean oxygen concentration was fixed ($C_{R0} = 30\%$) and we varied the oxygen gradient ($\Delta C_R = 0\%$ to 60%, i.e., from 30%–30% to 0%–60%). These experiments show that the CMC increases with the oxygen gradient (Figure 2c). Taken together, these two sets of results led us to hypothesize that *B. subtilis* senses the relative gradient of oxygen, $\nabla C/C$, or equivalently the gradient of the logarithm of oxygen concentration, $\nabla \log C$.

To test the hypothesis of logarithmic sensing, we computed the CMC for all experiments and studied its dependence on $\nabla C/C$. In this expression we used the mid-channel concentration C_0 for C, whereas ∇C is the same across the entire test channel. Results show that the CMC values over the entire set of 33 experiments collapse on a straight line when plotted against $\nabla C/C$ (Figure 3a), indicating that logarithmic-sensing underpins aerotaxis in *B. subtilis*. Evidence of logarithmic sensing in bacteria has to date been limited to the chemotaxis of *E. coli* to aspartate and serine,[23] where it was proposed to originate in methylation-mediated adaptation. For *B. subtilis*, our limited understanding of the intracellular dynamics underlying aerotaxis prevents us from speculating on the molecular underpinnings of logarithmic sensing, but the ability of the bacteria to rescale their aerotactic response in this manner and retain high sensitivity over a broad range of conditions indicates that aerotaxis is an important and fine-tuned behavioral response for this organism. The spread observed at $\nabla C/C = 4$/mm (Figure 3a) allows to identify the end of the logarithmic sensing regime, i.e., the maximum accumulation strength (i.e., higher CMC) is only observed for oxygen concentrations C_{R0} up to 1% (Figure 2a, inset and central plateau in Figure 3b) and rapidly decreases at higher concentrations.

Logarithmic sensing applies over a wide range of oxygen concentrations. To see this, we consider all experiments of the type 0%–*X*%, with *X* comprised between 0.01 and 100, which all have the same value of $\nabla C/C = 4$/mm (because both ∇C and C are proportional to *X*). The dependence of CMC for these experiments on the mid-channel concentration C_0 (Figure 3b) reveals a wide plateau ranging from $C_0 = 0.19$ μ mol/l to 73.0 μ mol/l where the CMC values are all within ± 7% of the mean CMC computed over this range (0.68). Taken together these results indicate that the magnitude of aerotaxis remains nearly unchanged over several orders of magnitude in oxygen concentration, provided $\nabla C/C$ is unchanged.

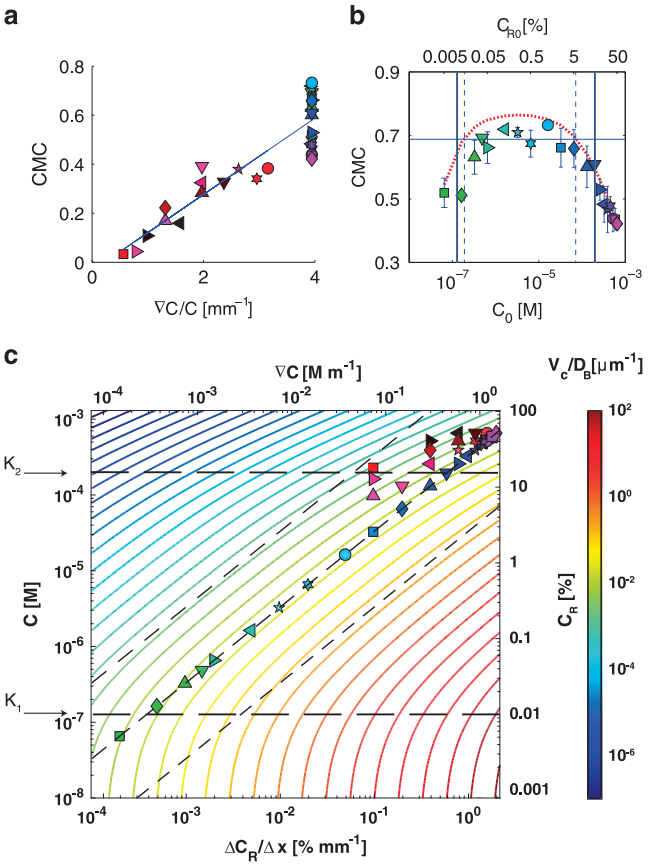

Figure 3. Logarithmic sensing in *B. subtilis* aerotaxis. (**a**) The Chemotactic Migration Coefficient (CMC) as a function of the relative gradient $\nabla C/C$. The solid line represents the best linear fit to the data. (**b**) The CMC for the experiments of the type 0%–*X*%, with *X* ranging from 0.01 to 100: all experiments in this set have the same oxygen gradient $\nabla C/C$, but different absolute concentrations C_{R0} (mid-channel concentration). Error bars represent s.e. calculated over the biological replicates (see Supplementary Table S1). The red dotted line is the CMC predicted by the model. The horizontal line denotes 90% of the maximum accumulation. Vertical solid lines represent K_1 and K_2 (equation (2)) as identified by the multi-experimental fitting procedure. Dashed blue lines delimit the region within which aerotactic accumulation was between 90% and 100% of the maximum. (**c**) Magnitude of the aerotactic response predicted by the model (equations (1 and 2)) over a broad range of oxygen concentrations C and concentration gradients ∇C, quantified in terms of the inverse of the accumulation length scale Vc/D_B. The measured bacteria diffusivity D_B was used (Supplementary Figure S2). Black dashed lines denote K_1 and K_2 and delimit the logarithmic sensing regime. Symbols correspond to experimental conditions and are as defined in Figure 1c).

A mathematical model of aerotaxis, informed by known elements of the biophysics of *HemAT*-mediated oxygen sensing, successfully predicts both the existence of logarithmic sensing and the concentration range over which it applies. Following an approach developed for state-driven stochastic processes with re-orientations,[24] we developed a one-dimensional advection diffusion model to predict the concentration of bacteria B(*x*,*t*), as

$$\frac{\partial B}{\partial t} = \frac{\partial}{\partial x}\left(D_B \frac{\partial B}{\partial x} - V_C(C, \nabla C)B\right) \quad (1)$$

where D_B is the diffusivity of the bacteria and V_C their chemotactic velocity. Analysis of cell trajectories in uniform oxygen

concentrations showed that the diffusivity, which results from the random component of motility, is nearly constant between oxygen concentrations of 390 μ mol/l and 1.3 m mol/l, and diminishes below 26 μ mol/l (Supplementary Figure S2; see Supplementary Information for an in-depth analysis). This leaves only the chemotactic velocity V_C to be determined in order to have a complete model of aerotaxis.

The fundamental element of the aerotaxis model is the functional dependence of V_C on the oxygen concentration C and concentration gradient ∇C. Although many different functional forms of V_C have been proposed, they nearly all fall in three categories: Keller–Segel models (KS), where $V_C = \chi_0 \nabla C/C$ and χ_0 is the chemotactic sensitivity coefficient; Lapidus–Schiller models (LS), where $V_C = \chi_0/(K+C)^2$ and K is the chemoreceptor-ligand dissociation constant; and Rivero–Tranquillo–Buettner–Lauffenburger models (RTBL), where $V_C = \frac{2}{3}V \tanh(\frac{K\chi_0}{2V}\nabla C/(K+C)^2)$ and V is swimming speed. Interestingly, although all these models have been developed to study chemotaxis in *E. coli*, they all fail to capture an important feature of chemotaxis in this microorganism: logarithmic sensing over a finite range of concentrations.[23] KS predicts logarithmic sensing (i.e., rescaling C by a constant leaves V_C unchanged) for any oxygen concentration, whereas neither LS nor RTBL support logarithmic sensing for any concentration.

We propose a new model for V_C that captures logarithmic sensing in *B. subtilis*' aerotaxis over a finite range of oxygen concentrations (Materials and Methods). We started from a one-dimensional Fokker-Planck model[24,25] to capture the temporal evolution of the spatial distribution of bacteria in an oxygen gradient (Supplementary Information, Supplementary Equation (5)), modeling the exploration of the one-dimensional domain as a velocity jump process, where bacteria can either run with constant speed in the positive or negative x direction, or tumble (i.e., instantaneously change direction). The probability of tumbling is controlled by an intracellular variable, the receptor methylation state, which in turn depends on the extracellular oxygen concentration (Supplementary Information, Supplementary Equation (54)). Moment closure and parabolic/hyperbolic scaling techniques then yielded (see Supplementary Information for the full derivation):

$$V_C = \chi_0 \frac{1}{(K_1 + C)(K_2 + C)} \nabla C \qquad (2)$$

where χ_0 is a chemotactic sensitivity coefficient as in the KS, LS and RTBL models and the oxygen concentrations K_1 and K_2 are traditionally interpreted as the dissociation constants for the receptor, which here is *HemAT*.[26] Importantly, K_1 and K_2 represent the boundaries of the logarithmic sensing regime, because for oxygen concentrations such that $K_1 \ll C \ll K_2$, equation (2) reduces to $V_C \approx (\chi_0/K_2)\nabla C/C$. Therefore, our model predicts logarithmic sensing in the range of concentrations delimited by K_1 and K_2, but not outside this range, in line with our experimental observations.

The model's ability to predict the observed bacterial distributions and the logarithmic sensing regime is not only qualitative, but also quantitative. We tested this by determining the concentrations K_1 and K_2 and the sensitivity χ_0 by fitting the steady-state version of equation (1)—with D_B from experiments (Supplementary Figure S2) and V_C from equation (2)—to the entire data set of 33 steady-state bacterial distributions, $B(x)$ (Figure 1b) (Materials and Methods). The best fit yielded $K_1 = 131$ n mol/l, $K_2 = 196$ μ mol/l and $\chi_0 = 1.43 \times 10^{-3}$ μm^2/s. For these parameter values the model predicts $B(x)$ accurately over the vast majority of the conditions tested, with an average error of 11% and only 1 out of 33 cases having an error $>30\%$, and thus accurately captures the dependence of the CMC on oxygen conditions (Figure 3b, red dashed line). An empirical verification of the extent of the logarithmic sensing regime can be obtained by determining the range of experiments in which the CMC was within 10% of the maximum (Figure 3b, region between the dashed blue lines). Given the structural properties of the model (see discussion above), we expect K_1 and K_2 to approximate the two boundaries of the logarithmic sensing regime. Indeed, we observe an excellent agreement between the inferred dissociation constants (Figure 3b, solid blue lines) and the empirical estimates.

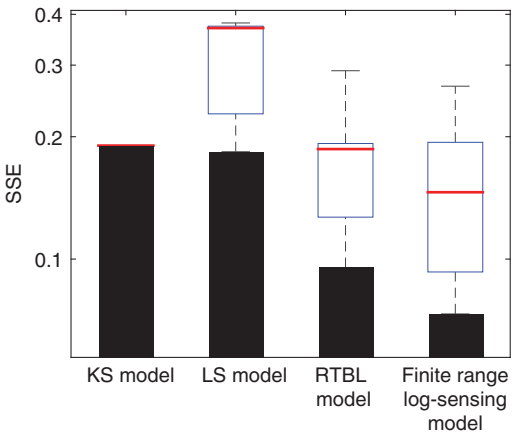

Figure 4. Error quantification in four classes of models for bacterial taxis, including the Keller–Segel model (KS), the Lapidus–Schiller model (LS), the Rivero–Tranquillo–Buettner–Lauffenburger model (RTBL), and the 'finite range log-sensing' model proposed here. For each model the graph shows the sum of the squared (weighted) errors (SSE, equation (5)) of the best solution identified among 100 iterations of the parameter optimization routine (black bars; Supplementary Information). The box plot summarizes the statistics of the 100 solutions obtained for each model: the median of the weighted SSE is in red, the extent of the blue box shows the first and last quartiles of the distribution, and the whiskers indicate the best and worst solution identified.

Repeating the fitting procedure to $B(x)$ for the three classes of chemotaxis models proposed to date (KS, LS and RTBL; Supplementary Information, Supplementary Figures S3–S5) showed that the 'finite range log-sensing' model proposed here is the one that best predicts our observations (Supplementary Table S1), with a 23%–61% lower prediction error than the other models (Figure 4). Two remarks have to be made in this context: (i) models with a larger number of parameters will tend perform better than models with fewer parameters (see Figure 4: both the models with 2 parameters, namely RTBL and Finite range log-sensing, perform consistently better than KS and LS) and (ii) we note that it was only possible to distinguish between the performance of different models owing to the low levels of noise in the observations brought about by the very large number of bacterial positions recorded (Figure 1c). We speculate that the noise intrinsic in most data sets on microbial taxis to date has prevented such a comparative model identification, highlighting the potential of image analysis for the accurate characterization of microbial taxis behaviors. This quantitative grounding of the model then allows one to apply it to predict the steady-state distributions of bacteria over the entire spectrum of oxygen concentrations and (linear) gradients (Figure 3c).

The most stringent validation of the model, which was derived based solely on steady-state data, was carried out by testing its performance in predicting the full aerotaxis dynamics in a transient experiment. In this experiment we exposed a *B. subtilis* population to a time-varying oxygen gradient beginning from uniform conditions (21%–21%) and ending after ~4 min with a gradient at low oxygen concentration (0%–0.05%) (Figure 5a). The spatial distribution of cells, $B(x,t)$, was tracked over time (Materials and Methods) as the oxygen gradient formed, showing bacteria migrating towards the higher oxygen region (Figures 5b and d). The timing of the onset

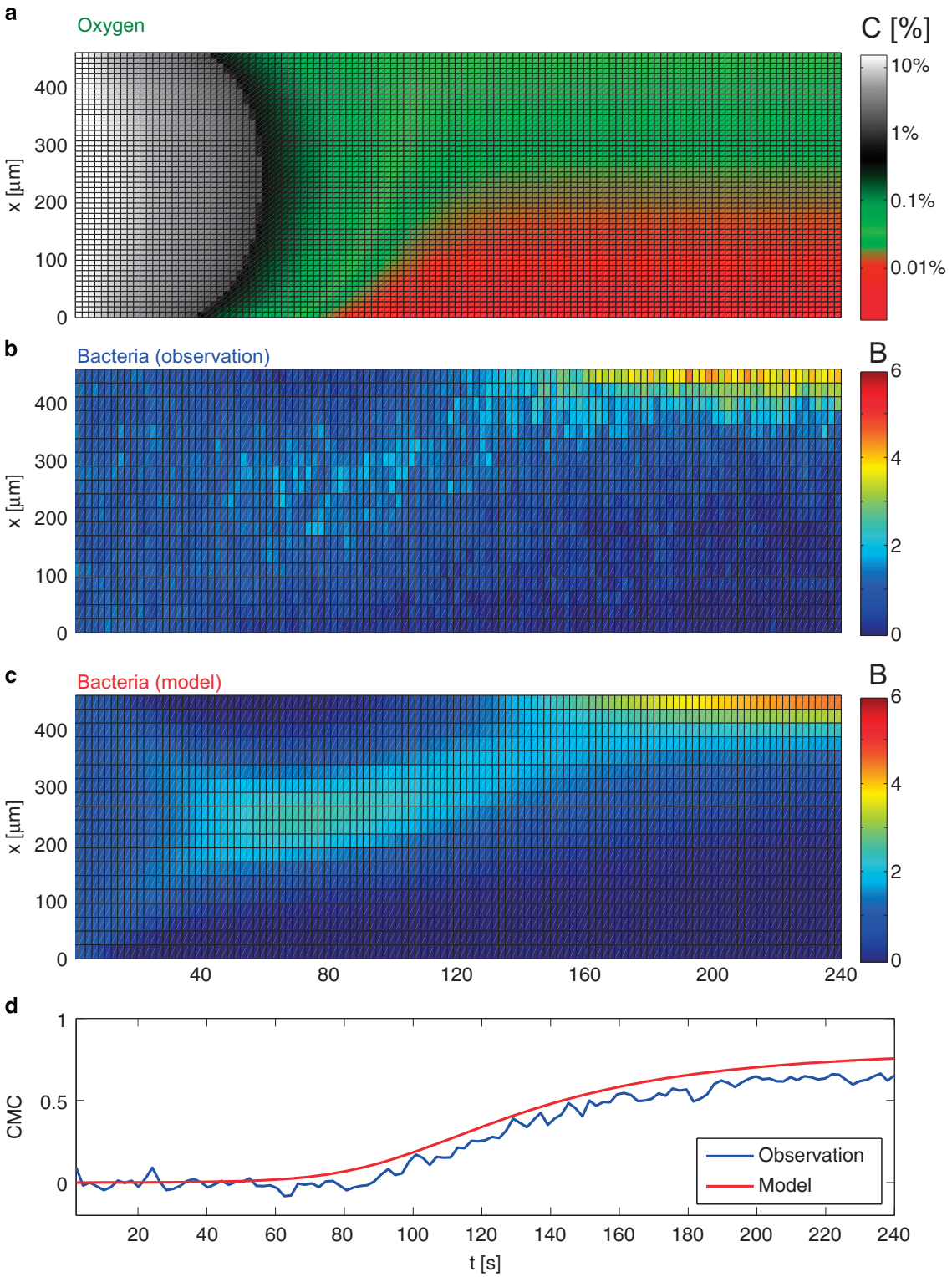

Figure 5. Validation of the 'finite range log-sensing' model on transient aerotaxis dynamics. (**a**) Simulated temporal evolution of the oxygen concentration across the test channel (x), as boundary conditions were changed from 21%–21% to 0%–0.05% oxygen saturation. (**b**) Observed and (**c**) predicted temporal evolution of the bacterial distribution across the test channel, $B(x)$. (**d**) Temporal evolution of the Chemotactic Migration Coefficient (CMC) for the observed (blue) and predicted (red) transient aerotaxis response.

and completion of this migration, as well as the magnitude of the resulting accumulation (CMC), were successfully captured by the model, composed of Equations (1) and (2) (Figures 5c and d). Differences in the resolution of the band between experiments and model were mostly due to the impossibility of collecting the same large amounts of data in these transient experiments as in the steady-state experiments, owing to the temporal evolution of the bacterial concentration profile. The overall good agreement confirms the ability of the model to capture not only the steady-state aerotactic response of *B. subtilis*, but also the transient.

CONCLUSIONS

We probed *B. subtilis*' aerotactic response in a wide range of oxygen gradients and concentrations, with exquisite precision in the quantification of cell distributions permitted by collection of very large data sets. Our results robustly demonstrate that, in contrast to previous findings,[1] *B. subtilis* always seeks the highest oxygen concentration available (Figure 2). Interestingly, we also observed that the strength of aerotaxis decreased above 20% oxygen—the maximum concentration of oxygen typically found in soil;[27] this also being a potential indicator of a mechanism to limit exposure to reactive oxygen species and oxidative damage.

Short of only being capable of exploiting oxygen-rich environments, observations in the quasi-anoxic and micro-oxic range revealed that *B. subtilis* is capable of exploiting shallow gradients at low oxygen concentrations, where it still displays strong aerotaxis. This behavior may underpin the escape from anoxic conditions, such as those prevalent in the intraluminal area of warm blooded animal guts.[28] This information is relevant in light of the recent identification of *B. subtilis* in mammalian microbiota.[29]

Our findings demonstrate that *B. subtilis* uses logarithmic sensing to measure and migrate in oxygen gradients and establishes the boundaries of the logarithmic sensing regime (Figures 2 and 3b). This property of chemoattractant signal transduction was previously found to underpin *E. coli*'s chemotaxis towards aspartate and serine.[23] Our results then demonstrate that logarithmic sensing is present in species of bacteria beyond *E. coli* and is not limited to chemotaxis but can also apply to aerotaxis. A recent study in *C. crescentus*, based on single-cell trajectory analysis, also suggested that aerotaxis in that species obeys logarithmic sensing, yet this conclusion was based on a single oxygen gradient.[6] Our comparison of different mathematical models suggests that such inferences of logarithmic sensing must be made with caution. Data over a broad range of oxygen conditions and a large number of cells are necessary to reliably distinguish between different models, and only some models support logarithmic sensing. Furthermore, the data-intensive approach presented here also provides information on the oxygen regime where logarithmic sensing applies, which is important in determining the role and occurrence of this rescaling behavior in natural environments.

Logarithmic sensing is particularly advantageous in the diffusion-dominated microscale world, where information about the position of an oxygen source is encoded in the shape of the oxygen field rather than in its absolute magnitude.[30] Furthermore, a wide range of oxygen concentrations and gradients are likely to characterize the natural habitats of *B. subtilis,* making logarithmic sensing an effective feature of a cosmopolitan lifestyle. We speculate that, by greatly improving the effectiveness of the bacterial search for essential compounds such as oxygen, logarithmic sensing in aerotaxis may be an important factor in the success and abundance of species such as *B. subtilis*.

MATERIALS AND METHODS

Design and execution of the experiments

B. subtilis strain OI1085 was obtained from George Ordal's laboratory. Cells from a frozen (−80 °C) stock were resuspended in 2 ml of Cap Assay Minimal media,[31] grown in a shaking incubator at 37 °C, 250 r.p.m. until the culture reached $OD_{600} = 0.3$. The bacterial suspension was then diluted 1:10 in fresh media before the injection into the microfluidic device (note that there were no modifications to the ambient air available to the cell cultures, see Methods in the Supplementary Information, Supplementary Figure S10 and the Supplementary Video). Cells were then exposed to the desired oxygen gradient by flowing mixtures of oxygen/nitrogen in the source and sink channels (Figures 1 and 5). For steady-state measurements of *B(x)* (Figure 1) cells were allowed to explore the gradient for 5 min and then 30 000 phase contrast micrographs were taken at intervals of 67 ms (such settings were empirically identified to provide the best compromise between a reasonable duration of each experiment, the accuracy in the estimate of *B*(*x*) and size of the resulting data set). To quantify the transient aerotactic response of *B. subtilis* (Figure 5) we injected cells in the test channel (21% oxygen flowing in the sink and source channels) and applied a 0% O_2 to the sink and 0.05% O_2 in the source. A video was then acquired at 100 frames per second for 4 min to locate cells during their migration in response to the developing oxygen gradient.

Data analysis and model identification

Single-cell coordinates were obtained from micrographs as previously described.[32] In the steady-state experiments all the coordinates from the 30 000 images acquired were pooled together to obtain the profiles plotted in Figure 1 (Supplementary Materials and Methods). For the model validation experiment, instead, the coordinates from 200 consecutive frames (acquired over 2 s) were pooled together to calculate a single *B(x)*, see Figure 5. The optimal parameters of the mathematical models included in this comparison were obtained via a fitting procedure accomplished using a Genetic Algorithm implemented in MATLAB. This routine was designed to explore the parameter space and identify the combination of parameter values that minimized the discrepancy, calculated as the weighted Sum of the Squared Error (SSE), between predicted and measured *B(x)* in response to a specific gradient profile (Supplementary Materials and Methods).

ACKNOWLEDGEMENTS

We thank Andrew Babbin, Francesco Carrara, Jeffrey S Guasto, Anupam Sengupta, Kwangmin Son, for stimulating discussions and George Ordal for supplying *Bacillus subtilis* OI1085. This work was supported by National Institutes of Health Grant 1R01GM100473-01 (to RS and EDS), by the Wellcome Trust-University of Edinburgh Institutional Strategic Support Fund and a Royal Society of Edinburgh—MoST grant (to FM).

COMPETING INTERESTS

The authors declare no conflict of interest.

REFERENCES

1. Taylor, B., Zhulin, I. & Johnson, M. Aerotaxis and other energy-sensing behavior in bacteria. *Annu. Rev. Microbiol.* **53**, 103–128 (1999).
2. Møller, M. M., Nielsen, L. P. & Jørgensen, B. B. Oxygen Responses and Mat Formation by *Beggiatoa* spp. *Appl. Environ. Microbiol.* **50**, 373–382 (1985).
3. Johnson, M. S., Zhulin, I. B., Gapuzan, M. E. & Taylor, B. L. Oxygen-dependent growth of the obligate anaerobe *Desulfovibrio vulgaris Hildenborough*. *J. Bacteriol.* **179**, 5598–5601 (1997).
4. Yao, J. & Allen, C. The plant pathogen *Ralstonia solanacearum* needs aerotaxis for normal biofilm formation and interactions with its tomato host. *J. Bacteriol.* **189**, 6415–6424 (2007).
5. Tamar, E., Koler, M. & Vaknin, A. The role of motility and chemotaxis in the bacterial colonization of protected surfaces. *Sci. Rep.* **6**, 19616 (2016).
6. Morse, M., Colin, R., Wilson, L. G. & Tang, J. X. The Aerotactic Response of *Caulobacter crescentus*. *Biophys. J.* **110**, 2076–2084 (2016).
7. Tuval, I. *et al.* Bacterial swimming and oxygen transport near contact lines. *Proc. Natl Acad. Sci. USA* **102**, 2277–2282 (2005).
8. Hillesdon, A. J., Pedley, T. J. & Kessler, J. O. The development of concentration gradients in a suspension of chemotactic bacteria. *Bull. Math. Biol.* **57**, 299–344 (1995).
9. Engelmann, T. W. Neue Methode zur Untersuchung der Sauerstoffausscheidung pflanzlicher und thierischer Organismen. *Pflügers Arch. Gesamte Physiol. Menschen Thiere* **25**, 285–292 (1881).
10. Wong, L. S., Johnson, M. S., Zhulin, I. B. & Taylor, B. L. Role of methylation in aerotaxis in *Bacillus subtilis*. *J. Bacteriol.* **177**, 3985–3991 (1995).
11. Wong, L. S. *Aerotaxis in Bacillus subtilis*. PhD thesis (1995).
12. Garrity, L. F. & Ordal, G. W. Chemotaxis in *Bacillus subtilis*: how bacteria monitor environmental signals. *Pharmacol. Ther.* **68**, 87–104 (1995).
13. Earl, A. M., Losick, R. & Kolter, R. Ecology and genomics of *Bacillus subtilis*. *Trends Microbiol.* **16**, 269–275 (2008).
14. Nakano, M. M. & Zuber, P. Anaerobic growth of a 'strict aerobe' (*Bacillus subtilis*). *Annu. Rev. Microbiol.* **52**, 165–190 (1998).
15. Mazzag, B. C., Zhulin, I. B. & Mogilner, A. Model of bacterial band formation in aerotaxis. *Biophys. J.* **85**, 3558–3574 (2003).

16. Adler, M., Erickstad, M., Gutierrez, E. & Groisman, A. Studies of bacterial aerotaxis in a microfluidic device. *Lab Chip* **12**, 4835–4847 (2012).
17. Bibikov, S. I., Barnes, L. A., Gitin, Y. & Parkinson, J. S. Domain organization and flavin adenine dinucleotide-binding determinants in the aerotaxis signal transducer Aer of *Escherichia coli*. *Proc. Natl Acad. Sci. USA* **97**, 5830–5835 (2000).
18. Rebbapragada, A. *et al.* The Aer protein and the serine chemoreceptor Tsr independently sense intracellular energy levels and transduce oxygen, redox, and energy signals for *Escherichia coli* behavior. *Proc. Natl Acad. Sci. USA* **94**, 10541–10546 (1997).
19. Alexandre, G. Coupling metabolism and chemotaxis-dependent behaviours by energy taxis receptors. *Microbiology* **156**, 2283–2293 (2010).
20. Zhulin, I. B., Bespalov, V. A., Johnson, M. S. & Taylor, B. L. Oxygen taxis and proton motive force in *Azospirillum brasilense*. *J. Bacteriol.* **178**, 5199–5204 (1996).
21. Ahmed, T., Shimizu, T. S. & Stocker, R. Microfluidics for bacterial chemotaxis. *Integr. Biol* **2**, 604 (2010).
22. Merkel, T. C., Bondar, V. I., Nagai, K., Freeman, B. D. & Pinnau, I. Gas sorption, diffusion, and permeation in poly(dimethylsiloxane). *J. Polym. Sci. Part B Polym. Phys.* **38**, 415–434 (2000).
23. Kalinin, Y. V., Jiang, L., Tu, Y. & Wu, M. Logarithmic sensing in *Escherichia coli* bacterial chemotaxis. *Biophys. J.* **96**, 2439–2448 (2009).
24. Grünbaum, D. Advection-diffusion equations for internal state-mediated random walks. *SIAM J. Appl. Math.* **61**, 43–73 (2000).
25. Wakano, J. Y., Nowak, M. A. & Hauert, C. Spatial dynamics of ecological public goods. *Proc. Natl Acad. Sci. USA* **106**, 7910–7914 (2009).
26. Zhang, W., Olson, J. & Phillips, G. N. Jr. Biophysical and kinetic characterization of HemAT, an aerotaxis receptor from *Bacillus subtilis*. *Biophys. J.* **88**, 2801–2814 (2005).
27. Lüdemann, H., Arth, I. & Liesack, W. Spatial changes in the bacterial community structure along a vertical oxygen gradient in flooded paddy soil cores. *Appl. Environ. Microbiol.* **66**, 754–762 (2000).
28. Espey, M. G. Role of oxygen gradients in shaping redox relationships between the human intestine and its microbiota. *Free Radic. Biol. Med.* **55**, 130–140 (2013).
29. Qin, J. *et al.* A human gut microbial gene catalog established by metagenomic sequencing. *Nature* **464**, 59–65 (2010).
30. Shoval, O. *et al.* Fold-change detection and scalar symmetry of sensory input fields. *Proc. Natl Acad. Sci. USA* **107**, 15995–16000 (2010).
31. Glekas, G. D. *et al.* Elucidation of the multiple roles of CheD in *Bacillus subtilis* chemotaxis. *Mol. Microbiol.* **86**, 743–756 (2012).
32. Rusconi, R., Guasto, J. S. & Stocker, R. Bacterial transport suppressed by fluid shear. *Nat. Phys.* **10**, 212–217 (2014).

Supplementary Information accompanies the paper on the *npj Systems Biology and Applications* website (http://www.nature.com/npjsba)

Supplementary Information

Filippo Menolascina[1,2], Roberto Rusconi[3,4], Vicente I. Fernandez[3,4], Steve P. Smriga[3,4], Zahra Aminzare[5], Eduardo D. Sontag[6] & Roman Stocker[3,4]

[1]*Institute for Bioengineering, School of Engineering, The University of Edinburgh, EH9 3DW Edinburgh, Scotland, UK*

[2]*SynthSys - Centre for Synthetic and Systems Biology, The University of Edinburgh, EH9 3BF Edinburgh, Scotland, UK*

[3]*Institute of Environmental Engineering, Department of Civil, Environmental and Geomatic Engineering, ETH Zurich, 8093 Zurich, Switzerland*

[4]*Ralph M. Parsons Laboratory, Department of Civil and Environmental Engineering, Massachusetts Institute of Technology, Cambridge, MA 02139, USA*

[5]*The Program in Applied and Computational Mathematic, Fine Hall, Washington Road, Princeton, NJ 08544, USA*

[6]*Department of Mathematics, Hill Center, 110 Frelinghuysen Rd, Rutgers, The State University of New Jersey, Piscataway, NJ 08854, USA*

SI Results

Oxgen diffusion within the device Oxygen diffusion within the microfluidic device was studied combining in-silico simulations and in-vitro experiments. To this aim a 1D model was developed

in COMSOL Multiphysics 4.4 (see Materials and Methods). Oxygen diffusion dynamics in the test channel were simulated for two gradients: 0%-20% and 0%-10% oxygen (dashed lines in Fig. S1). We then set out to quantify how the spatial profile of oxygen varied as a function of time for both gradients.

To measure oxygen concentrations in the test channel we flowed in the test channel a 167 ppm solution of ruthenium tris(2,2'-dypiridyl) dichloride hexahydrate (RTDP) in 66% ethanol in water, at a flow rate of 200 nL/min. RTDP is a fluorescent dye sensitive to oxygen: the larger the oxygen concentration, the smaller the intensity of the fluorescence that RTDP emits. Consistently with previous studies[16] we used the Stern-Volmer equation $I_0/I = 1 + K_q[\mathrm{O}_2]$ to convert the fluorescence intensity I in an oxygen concentration $[\mathrm{O}_2]$. First we need to estimate I_0, the fluorescence intensity in absence of oxygen (100% nitrogen) and the quenching constant K_q. To do so we flowed pure nitrogen (0% oxygen) in the source and sink channels, waited 10 minutes to make sure the gas concentration in the channel was equilibrated to uniform, and then acquired a fluorescence image of the channel. Background estimation and correction was carried out as in[16]; to this aim we extracted background fluorescence in the test channel fitting a second order polynomial across the x axis (i.e. the direction of the gradient) to intensities of areas 100 μm in the left and right PDMS walls -as there is no dye in the PDMS, and PDMS is not autofluorescent at the RTDP emission wavelength, we reasoned that any fluorescence in these areas can be classified as background. This procedure yielded an estimate of background fluorescence in the test channel -obtained using the fitted polynomial- that we used for correction by subtraction to all the intensity profiles we acquired[16]. As commonly noted, the quality of the micrographs decreased quickly in the vicinity

of PDMS walls; as this made a reliable measurements of signals very close to the boundaries of the test channel challenging, we decided to analyse oxygen concentrations between 10 and 450 μm. In the same manner we measured a second reference intensity, I_{air}, by flowing air (20.8% oxygen) in both the source and sink channels. This allowed us to calculate the quenching constant K_q by inverting the Stern-Volmer equation and plugging in the measurements of I_0 and $I = I_{air}$. This yielded$K_q = (I_0/I_{air} - 1)/20.8\% = 6.02$. With this value of K_q, any generic value of RTDP intensity I can be converted in an oxygen concentration solving the Stern-Volmer equation for the oxygen concentration, $[\mathrm{O}_2] = (I_0/I - 1)/K_q$.

To assess the accuracy of our mathematical model in predicting the spatiotemporal profile of oxygen, we generated (in two separate experiments) the two gradients simulated with our model, namely 0%-10% and 0%-20% oxygen. For each case, we quantified the background fluorescence, flowed in the source and sink the gas mixes appropriate to generate the desired gradient (e.g. nitrogen in the sink and 20% oxygen in the source for 0%-20%) and acquired fluorescence images every 10 seconds for 5 minutes. We then converted the fluorescence intensity values into oxygen concentrations with the procedure described above. The results of this approach are presented in Fig. S1 (solid line in panel A and squares in panel B). These measurements confirm that (i) the steady-state oxygen profile in the device is indeed linear, and (ii) both the steady-state (Fig. S1A) and the transients of oxygen diffusion (Fig. S1B) are well predicted by the mathematical model.

We note that, in the device used for our experiments, if we denote by O_{source} and O_{sink} the concentration (expressed in %) of oxygen flown in the source and sink channels, respectively, cells are exposed to $>$90% of the gradient from O_{sink} to O_{source}, and $<$10% of the gradient occurs within

the lateral PDMS boundaries separating the source and sink channels from the test channel. This can be easily observed in Table 1. When O_{source} =100% and O_{sink} =0%, the boundary conditions in the test channel are C(0 μm)= 6.04E-5 M, i.e. 4.7% of 1.3E-3 M (oxygen saturation in water in the lab), and C(460 μm)= 1.24E-3 M, i.e. 95.4% of 1.3E-3 M. This corresponds to a total drop in oxygen concentration within the test channel of ∼90.7%, to be compared to a 100% drop between the source and sink channels. This also means that $\sim 9.3\%$ of the gradient is retained in the PDMS walls and is not available to the cells.

Bacterial diffusivity D_B In order to measure the diffusivity of *B. subtilis* we tracked and analyzed bacterial trajectories in uniform concentrations of oxygen ranging from 0% to 100% (Fig. S2).The (2D projection) Mean Squared Displacement (MSD) of cell, subjected rotational can be written as:

$$\text{MSD}(t) = \frac{V^2\tau_R^2}{2}\left(\frac{2t}{\tau_R} + e^{-2t/\tau_R} - 1\right) \tag{1}$$

where V is cell's swimming speed, t is time and τ_R is the characteristic time-scale associated to rotational diffusion. We measure V directly (Fig. S2C) from bacterial trajectories and obtain τ_t and, therefore τ_R via fitting [33] ,[32]. In agreement with what has been reported in literature [34] we measure a tumbling time $\tau_t = \frac{1}{2}\tau_R \simeq 0.71s$ at low oxygen concentrations (O_2 <1%) and higher tumbling times $\tau_t \simeq 1.18s$ for $O_2 > 1\%$ (Fig. S2B). Consistently with previous reports our data also suggest the swimming speed increases with the concentration of oxygen (see Fig. S2C) up to ∼1% O_2. We can use these observations to derive the translational diffusion coefficient:

$$D_B = \frac{V^2\,\tau_t}{2} \tag{2}$$

We found that the translational diffusion coefficient shows a roughly constant value (336 μm^2/s) between 30% and 100% O_2. An additional constant D_B regime can be identified at lower O_2 concentration $D_B \simeq 181$ μm^2/s for 0%$<$ O_2 $\leq$1%, while at intermediate O_2 concentrations (1%$<$ O_2 $<$30%) D_B rapidly increases and decreases.

Mechanistic derivation of advection-diffusion equation In this section, we will show how an advection-diffusion equation for densities, of the type that we fit to data, might be reasonable. As little is known about the mechanistic basis of *B. subtilis* aerotaxis [35] our approach is as follows. We will first review an accepted and experimentally validated model of *E. coli*, and show how it leads to an advection-diffusion equation of the desired form. We will then see how this mechanism would be modified by incorporating knowledge about the differences between *E. coli* and *B. subtilis* chemotaxis, and we will show that the same advection-diffusion equation results in spite of this difference (albeit with very different parameters). As aerotaxis and chemotaxis in *B. subtilis* employs the same receptor mechanism [11], we will postulate that this same model applies to aerotaxis.

We organize this section by first discussing a general approach to advection-diffusion approximations, before specializing to the *E. coli* and *B. subtilis* models.

Preliminaries Let $p(x, y, \nu, t)$ be a density function describing a population of "particles" or agents (for example, bacteria), modeled in a $2N + m$ dimensional phase space, where at time t, $x = (x_1, \ldots, x_N) \in \mathbb{R}^N$ ($N = 1, 2, 3$; we soon specialize to $N = 1$) denotes the position of the agent, $y = (y_1, \ldots, y_m) \in Y \subset \mathbb{R}^m_{\geq 0}$ denotes the internal states of the agent (we will soon specialize to $m = 1$), and $\nu \in V \subset \mathbb{R}^N$ denotes its velocity. Also, $S(x) = (S_1, \ldots, S_M) \in \mathbb{R}^M$ denotes the concentration of signals in the environment which are sensed by each agent at space location x (we will soon specialize to $M = 1$). The external signal S is assumed to be constant in time (steady state assumption on chemoattractant), but is allowed to depend on space coordinates.

We assume that the following system of ordinary differential equations describes the evolution of the intracellular state, in the presence of the extracellular signal $S(x)$ at the current location of the agent:

$$\frac{dy}{dt} \;=\; f(y, \nu, S(x), S'(x)), \tag{3}$$

where $f\colon \mathbb{R}^m \times \mathbb{R}^N \times \mathbb{R}^M \times \mathbb{R}^M \to \mathbb{R}^m$ is a continuously differentiable function with respect to each component, i.e., $f \in C^1(\mathbb{R}^m \times \mathbb{R}^N \times \mathbb{R}^M \times \mathbb{R}^M)$. The derivative $S'(x)$ indicates derivative of S with respect to space (local gradient of chemoattractant). In most models, f depends explicitly only on y and S, but we allow this additional generality in the theory.

We assume also given an instantaneous reorientation ("tumbling") rate $\lambda = \lambda(y, S(x), S'(x))$ (often, λ depends only on certain combinations of y and $S(x)$, represented by the "activity" of re-

ceptors), the evolution of p is governed by the following transport (or "Fokker-Planck" or "forward Kolmogorov") equation [36] (omitting arguments of functions p and f, for readability):

$$\frac{\partial p}{\partial t} + \nabla_x \cdot \nu p + \nabla_y \cdot fp = -\lambda(y, S(x), S'(x))p + \int_V \lambda(y, S(x), S'(x))T(y, \nu, \nu')p(x, y, \nu', t)\, d\nu' \quad (4)$$

where the nonnegative kernel $T(y, \nu, \nu')$ is the probability that the agent changes the velocity from ν' to ν if a change of direction occurs. Also $\int_V T(y, \nu, \nu')\, d\nu = 1$.

The main goal here is to derive an approximate macroscopic model for chemotaxis using the microscopic model (4), i.e., we want to find an equation to approximately describe the evolution of the marginal density:

$$n(x, t) \;=\; \int_V \int_Y p(x, y, \nu, t)\, dy d\nu, \quad (5)$$

by adapting methods from Grunbaum [24] and Othmer [25]. We will assume that the external signal is isotropic in two state directions, so that in effect we can study one-dimensional motion.

A general equation in one dimension From now on, we study the movement of agents in one dimension have constant speed, so that the velocities are $\nu \in \{\bar{\nu}, -\bar{\nu}\}$, where $\bar{\nu}$ is a positive number, which we'll think of as a parameter in the equations. We will write $f^+(y, \bar{\nu}, S, S')$ instead of $f(y, \bar{\nu}, S, S')$ and $f^-(y, \bar{\nu}, S, S')$ instead of $f(y, -\bar{\nu}, S, S')$, and omit the bars from $\bar{\nu}$ from now

on. Similarly, for p, we let $p^{\pm}(x, y, t)$ denote the density of particles that at time t, are located at position x, with the internal state y, and with the constant speed ν, and moving to the right $(+)$ or left $(-)$ respectively.

The internal state evolves according to the following ODE system:

$$\frac{dy}{dt} \;=\; f^{\pm}(y, \nu, S, S'), \tag{6}$$

where $f^{\pm}\colon \mathbb{R}_{\geq 0} \times \mathbb{R} \times \mathbb{R} \times \mathbb{R} \to \mathbb{R}$ are continuously differentiable functions in each argument that describe the evolution of internal state of agents which move to the right $(+)$ and left $(-)$ respectively.

Note that we are allowing f to depend on the direction of movement as well as ν and S', the derivative of S with respect to space. In our examples, $f^{+} = f^{-}$ only depends on y and S, but we can consider the more general dependence in these preliminary derivations.

We describe the tumbling rate by introducing:

$$\lambda(y, S, S') \;= g(y, S, S'), \tag{7}$$

where g is a continuous function.

Then, according to Equation (4), $p^{\pm}(x, y, t)$ satisfy the following coupled first-order partial differ-

ential equations:

$$\frac{\partial p^+}{\partial t} + \nu \frac{\partial p^+}{\partial x} \; + \; \frac{\partial}{\partial y}\left[f^+(y,\nu,S,S')\; p^+ \right] \; = \; g(y,S,S')(-p^+ + p^-) \tag{8}$$

$$\frac{\partial p^-}{\partial t} - \nu \frac{\partial p^-}{\partial x} \; + \; \frac{\partial}{\partial y}\left[f^-(y,\nu,S,S')\; p^- \right] \; = \; g(y,S,S')(p^+ - p^-). \tag{9}$$

See [25] for existence and uniqueness of solutions of (8)-(9)

We assume given a forward-invariant set $I \subset \mathbb{R}_{\geq 0}$, i.e., if $y(0) \in I$, then $y(t) \in I$, for all $t \geq 0$, with the property that $p_0^{\pm}(x,y)$ are supported on I, i.e., $p_0^{\pm}(x,y) = 0$, when $y \notin I$. (In each of the examples to be considered below, such a set I will be constructed, by appealing to Lemma 1 in Section below). In other words,

$$p^{\pm}(x,y,t) = 0, \quad \forall x, y \notin I, t \geq 0. \tag{10}$$

The objective is to derive an approximate equation for the macroscopic density function

$$n(x,t) \; = \; \int_{\mathbb{R}_{\geq 0}} p^+(x,y,t) + p^-(x,y,t)\; dy, \tag{11}$$

using the microscopic model (8)-(9), by adapting a technique from [25]. To this end we introduce a flux variable j as well as moments associated to n and j:

$$
\begin{aligned}
j(x,t) &= \int_{\mathbb{R}\geq 0} \nu \left(p^+(x,y,t) - p^-(x,y,t)\right)\, dy, \\
n_i(x,t) &= \int_{\mathbb{R}\geq 0} y^i \left(p^+(x,y,t) + p^-(x,y,t)\right)\, dy, \quad \text{for} \quad i = 1,2,\ldots \\
j_i(x,t) &= \int_{\mathbb{R}\geq 0} y^i \nu \left(p^+(x,y,t) - p^-(x,y,t)\right)\, dy, \quad \text{for} \quad i = 1,2,\ldots.
\end{aligned} \tag{12}
$$

Note that by Equation (10) all the moments are well defined.

Next, we assume $f^+ = f_0 + \nu f_1$, and $f^- = f_0 - \nu f_1$, where the Taylor expansions of f_0 and f_1, with respect to the internal state y, are given as follows:

$$
f_0 = A_0 + A_1 y + A_2 y^2 + \cdots, \tag{13}
$$

$$
f_1 = B_0 + B_1 y + B_2 y^2 + \cdots, \tag{14}
$$

for some A_i's and B_i's that are functions of S, S', and ν^2. (We formally assume that these expansions exist.) Also we consider the following Taylor expansion for $g(y, S, S')$:

$$
g(y,S,S') = a_0 + a_1 y + a_2 y^2 + \cdots, \tag{15}
$$

where the a_i's are functions of S, and S'.

In addition, we assume $A_0 = 0$, because this is satisfied in our examples. Then by multiplying

(8) and (9) by 1, ν, and/or y, adding or subtracting, and integrating with respect to y on $\mathbb{R}_{\geq 0}$, and applying the fundamental theorem of calculus and integration by parts, we obtain the following equations for macroscopic density and flux and their first moments:

$$\frac{\partial n}{\partial t} + \frac{\partial j}{\partial x} = 0, \tag{16}$$

$$\frac{\partial j}{\partial t} + \nu^2 \frac{\partial n}{\partial x} = -2a_0 j - 2a_1 j_1 - 2\sum_{k\geq 2} a_k j_k, \tag{17}$$

$$\frac{\partial n_1}{\partial t} + \frac{\partial j_1}{\partial x} = B_0 j + A_1 n_1 + B_1 j_1 + \sum_{k\geq 2} A_k n_k + \sum_{k\geq 2} B_k j_k, \tag{18}$$

$$\begin{aligned}\frac{\partial j_1}{\partial t} + \nu^2 \frac{\partial n_1}{\partial x} &= \nu^2 B_0 n + \nu^2 B_1 n_1 + (A_1 - 2a_0) j_1 \\ &\quad + \nu^2 \sum_{k\geq 2} B_k n_k + \sum_{k\geq 2} (A_k - 2a_{k-1}) j_k\end{aligned} \tag{19}$$

Note that by Equation (10), $p^{\pm} = 0$ outside the interval I, therefore, for any $i = 0, 1, \ldots$

$$\lim_{y\to\infty} y^i (p^+ \pm p^-) = 0, \quad \lim_{y\to 0} y^i (p^+ \pm p^-) = 0.$$

Parabolic scaling

In this section, we introduce a parabolic scaling to derive an approximate chemotaxis equation from the moment equations (16)-(19). Let L, T, ν_0, y_0, and N_0 be scale factors for the length, time, velocity, internal state, and particle density respectively, and define the following dimensionless

parameters (we use hats to denote the dimensionless forms of the parameters):

$$\hat{\nu} \;=\; \frac{\nu}{\nu_0}, \quad \hat{y} = \frac{y}{y_0}, \tag{20}$$

$$\hat{n} \;=\; \frac{n}{y_0 N_0}, \quad \hat{\hat{j}} \;=\; \frac{j}{y_0 N_0 \nu_0}, \tag{21}$$

$$\hat{n}_i \;=\; \frac{n_i}{y_0^{i+1} N_0}, \quad \hat{\hat{j}}_i \;=\; \frac{j_i}{y_0^{i+1} N_0 \nu_0}, \quad \text{for} \quad i = 1, 2, \ldots \tag{22}$$

$$\hat{a}_i \;=\; y_0^i T\, a_i, \quad \hat{A}_i \;=\; y_0^{i-1} T\, A_i, \quad \hat{B}_i \;=\; y_0^{i-1} L\, B_i, \quad \text{for} \quad i = 0, 1, \ldots \tag{23}$$

The parabolic scales of space and time are given by:

$$\hat{x} \;=\; \left(\frac{\epsilon L}{\nu_0 T}\right) \frac{x}{L}, \quad \hat{t} \;=\; \epsilon^2 \frac{t}{T}, \tag{24}$$

for any arbitrary ϵ.

Now assume that under appropriate conditions to be verified in particular examples, for any $i \geq 2$, the j_i's and n_i's are much smaller than j_1 and n_1 and can be neglected. (For example see the definition of shallow gradient in Example below.)

Therefore, the dimensionless form of moment equations (16)-(19), for $\epsilon = \dfrac{T\nu_0}{L}$, become:

$$\epsilon^2 \frac{\partial \hat{n}}{\partial \hat{t}} + \epsilon \frac{\partial \hat{j}}{\partial \hat{x}} = 0, \tag{25}$$

$$\epsilon^2 \frac{\partial \hat{j}}{\partial \hat{t}} + \epsilon \hat{\nu}^2 \frac{\partial \hat{n}}{\partial \hat{x}} = -2\hat{a}_0 \hat{j} - 2\hat{a}_1 \hat{j}_1, \tag{26}$$

$$\epsilon^2 \frac{\partial \hat{n}_1}{\partial \hat{t}} + \epsilon \frac{\partial \hat{j}_1}{\partial \hat{x}} = \epsilon \hat{B}_0 \hat{j} + \hat{A}_1 \hat{n}_1 + \epsilon \hat{B}_1 \hat{j}_1, \tag{27}$$

$$\epsilon^2 \frac{\partial \hat{j}_1}{\partial \hat{t}} + \epsilon \hat{\nu}^2 \frac{\partial \hat{n}_1}{\partial \hat{x}} = \epsilon \hat{\nu}^2 \hat{B}_0 \hat{n} + \epsilon \hat{\nu}^2 \hat{B}_1 \hat{n}_1 + (\hat{A}_1 - 2\hat{a}_0) \hat{j}_1. \tag{28}$$

Next, we write Equations (25)-(28) in a matrix form, as follows:

$$\epsilon^2 \frac{\partial \hat{w}}{\partial \hat{t}} + \epsilon \frac{\partial}{\partial \hat{x}} P\hat{w} = \epsilon Q\hat{w} + R\hat{w}, \tag{29}$$

where $\hat{w} = \left(\hat{n}, \hat{j}, \hat{n}_1, \hat{j}_1\right)^T$ and the matrices P, Q, and R defined as follows:

$$P = \begin{pmatrix} 0 & 1 & 0 & 0 \\ \hat{\nu}^2 & 0 & 0 & 0 \\ 0 & 0 & 0 & 1 \\ 0 & 0 & \hat{\nu}^2 & 0 \end{pmatrix}, Q = \begin{pmatrix} 0 & 0 & 0 & 0 \\ 0 & 0 & 0 & 0 \\ 0 & \hat{B}_0 & 0 & \hat{B}_1 \\ \hat{\nu}^2 \hat{B}_0 & 0 & \hat{\nu}^2 \hat{B}_1 & 0 \end{pmatrix}, R = \begin{pmatrix} 0 & 0 & 0 & 0 \\ 0 & -2\hat{a}_0 & 0 & -2\hat{a}_1 \\ 0 & 0 & \hat{A}_1 & 0 \\ 0 & 0 & 0 & \hat{A}_1 - 2\hat{a}_0 \end{pmatrix}.$$

Assuming the regular perturbation expansion for w,

$$\hat{w} = \hat{w}^0 + \epsilon \hat{w}^1 + \epsilon^2 \hat{w}^2 + \ldots, \quad \text{where} \quad \hat{w}^i = \left(\hat{n}^i, \hat{j}^i, \hat{n}_1^i, \hat{j}_1^i\right)^T,$$

and comparing the terms of equal order in ϵ in (29), we get:

$$\epsilon^0: \quad R\hat{w}^0 \;=\; 0 \quad \Rightarrow \quad \hat{w}^0 \;=\; (\hat{n}^0, 0, 0, 0)^T \tag{30}$$

$$\epsilon^1: \quad R\hat{w}^1 \;=\; -Q\hat{w}^0 + \frac{\partial}{\partial \hat{x}} P\hat{w}^0$$

$$\Rightarrow \quad \begin{pmatrix} 0 \\ -2\hat{a}_0\hat{j}^1 - 2\hat{a}_1\hat{j}_1^1 \\ \hat{A}_1\hat{n}_1^1 \\ (\hat{A}_1 - 2\hat{a}_0)\hat{j}_1^1 + \hat{\nu}^2\hat{B}_0\hat{n}^0 \end{pmatrix} = \begin{pmatrix} 0 \\ \hat{\nu}^2\frac{\partial}{\partial \hat{x}}\hat{n}^0 \\ 0 \\ 0 \end{pmatrix}. \tag{31}$$

From the last equality of Equation (31), we can derive the following equation for $\hat{j}_1^1$:

$$\hat{j}_1^1 \;=\; -\frac{\hat{\nu}^2\hat{B}_0}{\hat{A}_1 - 2\hat{a}_0}\hat{n}^0.$$

By substituting $\hat{j}_1^1$ into the second equality of Equation (31), we obtain the following equation

$$\hat{j}^1 \;=\; -\frac{\hat{\nu}^2}{2\hat{a}_0}\frac{\partial \hat{n}^0}{\partial \hat{x}} + \frac{\hat{a}_1\hat{B}_0\hat{\nu}^2}{\hat{a}_0(\hat{A}_1 - 2\hat{a}_0)}\hat{n}^0. \tag{32}$$

Now we compare the terms with order ϵ^2:

$$\epsilon^2: \quad R\hat{w}^2 \;=\; -Q\hat{w}^1 + \frac{\partial}{\partial \hat{x}} P\hat{w}^1 + \frac{\partial}{\partial \hat{t}}\hat{w}^0. \tag{33}$$

Note that $(1, 0, 0, 0)^T$ is in the kernel of R and the right hand side of (33) is in the image of R.

Therefore their inner product is zero:

$$\frac{\partial}{\partial \hat{x}} \hat{j}^1 + \frac{\partial}{\partial \hat{t}} \hat{n}^0 \;=\; 0. \tag{34}$$

Equation (32) together with Equation (34) give the following equation for n^0 in the dimensionless variables:

$$\frac{\partial \hat{n}^0}{\partial \hat{t}} \;=\; \frac{\partial}{\partial \hat{x}} \left(\frac{\hat{\nu}^2}{2\hat{a}_0} \frac{\partial \hat{n}^0}{\partial \hat{x}} - \frac{\hat{a}_1 \hat{B}_0 \hat{\nu}^2}{\hat{a}_0(\hat{A}_1 - 2\hat{a}_0)} \hat{n}^0 \right). \tag{35}$$

Since $n(x,t) = n^0(x,t) + \mathcal{O}(\epsilon)$, if we neglect the $\mathcal{O}(\epsilon)$ term, Equation (35) leads to the following chemotaxis equation in dimensionless variables:

$$\frac{\partial \hat{n}}{\partial \hat{t}} \;=\; \frac{\partial}{\partial \hat{x}} \left(\frac{\hat{\nu}^2}{2\hat{a}_0} \frac{\partial \hat{n}}{\partial \hat{x}} - \frac{\hat{a}_1 \hat{B}_0 \hat{\nu}^2}{\hat{a}_0(\hat{A}_1 - 2\hat{a}_0)} \hat{n} \right). \tag{36}$$

Changing back to the original (dimensional) variables, we obtain the following PDE:

$$\frac{\partial n}{\partial t} \;=\; \frac{\partial}{\partial x} \left(\frac{\nu^2}{2a_0} \frac{\partial n}{\partial x} - \frac{a_1 B_0 \nu^2}{a_0(A_1 - 2a_0)} n \right). \tag{37}$$

Examples

E.coli

The following simplified one-dimensional model provides a phenomenologically accurate model of the chemotactic response of *E.coli* bacteria to MeAsp; see for example [39], [37]. The internal state evolves according to an ordinary differential equation:

$$\frac{dm}{dt} = K_r(1-a) - K_b a$$

which describes the methylation state of receptors, where a is a number between 0 and 1 that quantifies the fraction of active receptors, and is written as follows:

$$a = \frac{1}{1+(F_m F_l)^N}$$

in terms of free energy differences due to methylation and ligand respectively:

$$F_m = \exp(\alpha(1-m))\,, \qquad F_l = \frac{1+S/K_I}{1+S/K_A}\,,$$

where K_I and K_A are dissociation constants for inactive and active Tar receptors, respectively. This arises from an MWC [38] model of clusters of N receptors that rapidly switch between active and inactive states, In summary, we write:

$$a = \frac{1}{1 + K\left(\dfrac{S + K_I}{(S + K_A)\, y}\right)^N}$$

and K, K_I, and K_A are nonnegative constants and $K_I < K_A$.

With appropriate parameter choices [39], [37], this model fits very well the response of *E. coli* to the ligand α-methylaspartate.

E. coli tumbling rate is controlled by the concentration of cheY-P. In this simplified model, one thinks of phosphorylation state of cheY as directly proportional to activity, assuming fast phosphotransfer. Thus, one takes the jump (or "tumbling" for bacteria) rate in the form:

$$\lambda(y, S) \;=\; \frac{1}{\tau}\left(\frac{a}{a_0}\right)^H .$$

Here a_0 denotes a steady-state kinase activity, H a motor amplification coefficient, and τ the average run time. We write

$$\lambda(y, S) \;=\; R a^H, \tag{38}$$

where $R = (\tau a_0^H)^{-1}$.

It is convenient to use $y = e^{\alpha m}$ as a state variable, instead of the methylation level m. So the

equations can be rewritten as follows:

$$\frac{dy}{dt} \;=\; \alpha y\left(K_r(1-a) - K_b a\right) \;=\; py(q-a), \tag{39}$$

provided that we pick

$$p = \alpha(K_r + K_b)\,, \quad q = \frac{K_r}{K_r + K_b}\,.$$

Observe that $F_m = e^{\alpha}/y$ when expressed in terms of the new variable y. The parameters p, q, K, N, and H are all positive, and, from its definition, it is clear that q is between 0 and 1.

The objective is to derive a parabolic equation for the macroscopic density function. It is convenient to define a new internal state variable as follows:

$$w \;=\; p(a-q). \tag{40}$$

Then, a simple calculation shows that

$$\frac{dw}{dt} \;=\; \frac{N}{p}(w+pq)(w+pq-p)\left(w \pm \frac{\nu S'\left(K_A - K_I\right)}{\left(K_A+S\right)\left(K_I+S\right)}\right), \tag{41}$$

and

$$\lambda(w) \;=\; \frac{R}{p^H}(w+pq)^H. \tag{42}$$

For convenience of notation, let us define $G(S) := \log\left(\dfrac{S+K_I}{S+K_A}\right)$.

Lemma 1. *Let* $c = \min\{pq, p-pq\}$. *If* $|G'(S)| \le \frac{c}{\nu}$ *and* $|w(0)| \le c$, *then* $|w(t)| \le c$ *for all* $t \ge 0$.

See [57] for a proof.

Let L, T, ν_0, and N_0 be scale factors for the length, time, velocity, and particle density respectively, and define the following dimensionless quantities: A simple calculation shows that:

$$\begin{aligned} &G'(S)\widehat{G'(S)} \;=\; LG'(S), \quad \hat{N} \;=\; N, \quad \hat{p} \;=\; Tp, \quad \hat{w} = Tw, \quad \hat{q} \;=\; q \\ &\hat{R} \;=\; TR, \quad \hat{K}_A = \frac{K_A}{L}, \quad \hat{K}_I = \frac{K_I}{L}, \quad \hat{z} = Tz. \end{aligned} \tag{43}$$

All other parameters remain the same as in Equations (20)-(22), and Equation (24), for $y_0 = \frac{1}{T}$.

Note that for $\epsilon = \dfrac{\nu_0 T}{L}$, we have the following analogous result to Lemma 1, in hyperbolic scale:

$$\left|G'(S)\widehat{G'(S)}\right| \;\le\; \frac{\hat{c}}{\hat{\nu}}\frac{1}{\epsilon}, \quad \hat{w}(0) \le \hat{c} \quad \Rightarrow \quad \hat{w}(t) \le \hat{c}, \;\; t > 0. \tag{44}$$

Definition 1 (shallow condition)**.** *If* $\left|G'(S)\widehat{G'(S)}\right| \;\le \bar{K}$, *where* $\bar{K} = \mathcal{O}(1)$, *we say* S *has a shallow gradient.*

Lemma 2. *Assume that*

$$\left|G'(S)\widehat{G'(S)}\right| \leq \frac{\hat{c}}{\hat{\nu}}, \tag{45}$$

i.e., S has a shallow gradient. Then, for any $i \geq 1$,

$$\frac{\hat{j}_i}{\hat{n}} \leq \mathcal{C}_i \epsilon^i, \quad \textit{and} \quad \frac{\hat{n}_i}{\hat{n}} \leq \mathcal{D}_i \epsilon^i,$$

for some constants $\mathcal{C}_i = \mathcal{O}(1)$, and $\mathcal{D}_i = \mathcal{O}(1)$.

See [57] for a proof.

Remark 1. Equation (45) is equivalent to the following condition for $G'(S)$:

$$|G'(S)| \leq \frac{c}{\nu}\epsilon, \tag{46}$$

or equivalently

$$\frac{\nu}{c}\left|\frac{(K_A - K_I)\, S'}{(S + K_A)\,(S + K_I)}\right| \leq \epsilon. \tag{47}$$

Note that for exponential signal $S(x) = e^{\rho x}$, using condition (47), when ρ is small enough, we are in a shallow gradient regime. For linear signal $S(x) = ax + b$, using condition (47), when a is small enough, we are in a shallow gradient regime.

Using the notations of Equations (13)-(14),

$$A_0 \;=\; 0, \quad A_1 \;=\; Npq\,(q-1)\,, \quad B_0 \;=\; Npq\,(q-1)\,\frac{S'\,(K_A-K_I)}{(K_A+S)\,(K_I+S)}.$$

In order to derive an advection-diffusion approximation using Equation (37), we just need to find the first two terms of the Taylor expansion of $\lambda(w)$ in (42). We do that next.

A simple calculation shows that

$$\lambda(w) \;=\; Rq^H \;+\; \frac{HRq^H}{pq}w + Q(w),$$

where $Q(w)$ is the sum of higher orders of w in the Taylor expansion. Plugging the new values of a_0 and a_1 into Equation (37), we get the following advection diffusion equation:

$$\frac{\partial n}{\partial t} \;=\; \frac{\partial}{\partial x}\left(D\frac{\partial n}{\partial x} - Vn\right), \tag{48}$$

where

$$D = \frac{\nu^2}{2Rq^H}, \quad \text{and} \quad V(x) = \frac{(K_A-K_I)\,S'(x)}{(K_A+S(x))\,(K_I+S(x))}V_0$$

with

$$V_0 = \frac{NH\,(1-q)\,\nu^2}{Npq\,(1-q) + 2Rq^H}.$$

Modifications for *B. subtilis*

It is known that the activity of *B. subtilis* chemotatic receptors increases in the presence of attractants. This means, in effect, that the roles of K_I and K_A are inverted in the formula for activity: now $K_I > K_A$. Furthermore, tumbling (due to CW rotation of flagella) is induced by lack of activity, which we may model by replacing a by the fraction of inactive receptors, $1 - a$, in the simplified *E. coli* model considered earlier.

Thus, we now assume that the internal state evolves according to the following ODE system:

$$\frac{dy}{dt} \;=\; py(q-a), \tag{49}$$

where we use the following form for activity:

$$a = \frac{1}{1 + K\left(\dfrac{S + K_I}{(S + K_A)\,y}\right)^N}$$

and p, q, K, and N, K_I, and K_A are positive constants, where now $K_I > K_A$. Recall that q is between zero and one.

We assume now the following form for the tumbling rate:

$$\lambda(y, S) \;=\; R(A - a)^H, \tag{50}$$

where A and R are positive constants. (We assume that $A > q$, which is the case if $A = 1$.)

The objective is to derive a parabolic equation for the macroscopic density function.

As in the previous example, let $w \;=\; p(a - q)$. Then, a simple calculation shows that

$$\begin{aligned} \frac{dw}{dt} \;&=\; \frac{N}{p}(w + pq)(w + pq - p)\left(w \pm \frac{\nu S'\left(K_A - K_I\right)}{\left(K_A + S\right)\left(K_I + S\right)}\right) \\ \lambda(w) \;&=\; \frac{R}{p^H}(pA - pq - w)^H. \end{aligned} \tag{51}$$

Since $\frac{dw}{dt}$ is exactly the same as in Example , we get the same expressions for A_i's and B_i's, namely:

$$A_0 \;=\; 0, \quad A_1 \;=\; Npq\left(q - 1\right), \quad B_0 \;=\; Npq\left(q - 1\right)\frac{S'\left(K_A - K_I\right)}{\left(K_A + S\right)\left(K_I + S\right)}. \tag{52}$$

In order to derive an advection-diffusion approximation using Equation (37), we just need to find the first two terms of the Taylor expansion of $\lambda(w)$. We do that next.

A simple calculation shows that

$$\lambda(w) \;=\; R(A-q)^H - \frac{RH}{p}(A-q)^{H-1}w + Q(w),$$

where $Q(w)$ is the sum of higher orders of w in the Taylor expansion. Plugging the new values of a_0 and a_1 into Equation (37), we get the following advection diffusion equation:

$$\frac{\partial n}{\partial t} \;=\; \frac{\partial}{\partial x}\left(D\frac{\partial n}{\partial x} - Vn\right), \tag{53}$$

where

$$D \;=\; \frac{\nu^2}{2R(A-q)^H}, \quad \text{and} \quad V \;=\; \frac{(K_I-K_A)S'(x)}{(K_A+S)(K_I+S)}V_0,$$

with

$$V_0 \;=\; \left(\frac{1-q}{A-q}\right)\frac{NqH\nu^2}{Npq(1-q)+2R(1-q)^H},$$

that can be also rearranged in a more compact form, gives us Equation (2) as presented in the main text:

$$V_C = \frac{\chi_0}{(K_1+C)(K_2+C)}C' \tag{54}$$

with

$$V_C = V, K_1 = K_I, K_2 = K_A, C = S\chi_0 = V_0(K_I - K_A).$$

Thus, a formula of exactly the same form as for *E. coli* has been obtained.

Our mathematical model best captures aerotaxis in B. subtilis In order to assess how the model we propose compares to alternative solutions in literature we grouped previous advection-diffusion chemotaxis models in 3 main classes: KS, LS and RTBL models (see following section). Each of these models has a different expression of the chemotactic speed V_C and they range from fully phenomenological (e.g. KS) to biophysically-informed approaches (like RTBL). The vast majority of the other advection-diffusion models used to capture chemotaxis can be derived from the ones we consider in the following.

We compared the performance of the models by plotting the prediction (Fig. S3-S9) of the best combination of parameters the optimization algorithm found over 100 iterations and its prediction error (Fig. 5, see Eq. 5 in the main text). For each model we also plot the distribution of prediction errors of the 100 solutions to the optimization problem.

Notably, for the KS model the genetic algorithm consistently identified a single solution to the parameter optimization problem (Fig. S3), hence the tight distribution in Fig. 5. Similar results in terms of prediction accuracy (and therefore SSE, see Fig. 5) can be achieved using the best solution identified for the LS model (Fig. S4). A significant improvement, instead, can be achieved using

the RTBL model (Fig. S5 and Fig. 5): the best parameter set found in this case achieves an SSE significantly smaller than in the previous cases ($0.95 \cdot 10^{-1}$ compared to $1.84 \cdot 10^{-1}$ for the LS and $1.90 \cdot 10^{-1}$ for the KS models). However the model we propose displays the smallest prediction error ($0.73 \cdot 10^{-1}$, Fig. 5) and therefore best captures the body of experimental data we describe (Fig. 1C).

1 SI Materials and Methods

Growth protocol

B. subtilis strain OI1085 cells from a frozen (-80°C) stock were resuspended in 2 mL of Cap Assay Minimal media (50 mM KH2PO4, 50 mM K2HPO4, 1 mM MgCl2, 1 mM NH4SO4, 0.14 mM CaCl2, 0.01 mM MnCl2, 0.20 mM MgCl2), adding 15 μL HMT (5 mg/mL each of histidine, methionine, and tryptophan, filter sterilized), 50 muL Tryptone Broth (10 g Tryptone (Difco) and 5 g NaCl in 1 L of distilled water), and 50 μL 1 M Sorbitol (filter sterilized). The culture was incubated at 37°C while shaking at 250 rpm until OD600 = 0.3 was reached. The culture was then diluted 1:10 in fresh media before injection in the microfluidic device, to ensure cells were in sufficiently low abundance to not affect the oxygen gradient via respiration.

2 Microfluidic fabrication, experimental operation and image analysis

In order to generate oxygen gradients, the source and sink channels were each connected to a gas-mixing unit, supplied by gas tanks (Air Gas, MA). We used 100% nitrogen as well as 0.1%, 1%, 20% and 100% oxygen/nitrogen mixtures. Each gas-mixing unit was composed of two high-precision flow controllers (Cole Parmer, IL), one for the appropriate mixture of oxygen and the other for nitrogen, controlled by a MATLAB routine to achieve the final oxygen concentration that would be flown into the source or sink channel. The sum of the flow rates in each line was set to 10 mL/min, while the ratio was set to achieve the desired oxygen concentration. The outlets of the two flow controllers in each mixer were connected using a Y-junction, and low oxygen permeability tubing (C-flex Ultra, Cole Parmer, IL) was used to connect all the components to the microfluidic device. To fabricate the microfluidic device we devised a precision cutting strategy based on piezoelectric actuation to remove three 38 mm-long bands from a 200 μm thick PDMS sheet. This yielded three parallel grooves piercing through the full depth of the PDMS sheet: the central one ('test channel', 460 μm wide) was separated from each of the flanking ones ('sink channel' and 'source channel') by a 220 μm thick PDMS wall. We then used a handheld plasma bonder (BD20AC, ETP) to irreversibly bond the PDMS structure to two 2x3 inch glass slides, one at the top and one at the bottom. Inlets and outlets were obtained by drilling holes ($\oslash$=1 mm) in the glass slides before bonding. In a typical experiment, we flowed the desired oxygen mixtures in the source and sink channels and allowed them to diffuse within the device. Of note, the presence of the 220 μm thick PDMS wall separating the test channel from the sink channel implied that the minimum oxygen concentration in the test channel was higher than the concentration in

the sink channel. Similarly, the maximum concentration in the test channel was lower than the concentration in the source channel. For example, a 0%-100% case (0 M in the sink channel and ≈ 8 mM, on the other end, at the interface between PDMS and the source channel) corresponds to an oxygen gradient ranging from 4.6% (60 μM) to 95% (1.24 mM, 100% oxygen in water corresponding to 1.3 mM) in the test channel (see Table 1 in the Supplementary Information). Bacteria were then injected in the test channel and glass coverslips were used to seal its inlet and outlet of the test channel to suppress any residual flow. Cells reached steady state distribution within 5 minutes after the injection (Fig. 4). We then used an automated acquisition routine to capture 30,000 phase-contrast images of the same location along the test channel (equidistant from the inlet and outlet) at 67 ms intervals over 33 min (20 objective; Andor Zyla camera with 6.5 μm/pixel (leading to 0.33 μm/pixel resolution); see Materials and Methods). Each image contained 30-80 individual cells, making for (1-3)$\cdot 10^6$ total recorded cell positions and an estimated 380-1020 individual bacteria included in the analysis. From these, we quantified the concentration of bacteria $\mathrm{B}(x)$ in the direction x across the channel, normalized to a mean of 1 for comparison among different conditions (see Materials and Methods; Fig. 1C). The large number of bacterial positions recorded in each experiment enabled the quantification of $\mathrm{B}(x)$ with a spatial (x) resolution of 4.6 μm and minimal noise (Fig. 1B,C), which proved fundamental for robust model identification. We imaged the bacteria at channel mid-depth using an inverted microscope (Eclipse TE2000-E; Nikon) with a 20 phase-contrast objective (NA = 0.45) and an sCMOS camera (Andor Zyla). A custom MATLAB (Mathworks, MA) algorithm was used for image analysis to accurately identify individual cell coordinates. The normalized bacterial concentration, $\mathrm{B}(x)$, was obtained from the histogram

of the number of bacteria in one hundred bins along the x direction, each 4.6 μm wide and together covering the 460 μm width of the test channel, and then normalizing this distribution to a mean of 1. The uncertainty in the estimate of $\mathrm{B}(x)$ was obtained via bootstrapping bacterial x coordinates from all the experiments available for each of the 33 gradients were pooled together. One million samples of 10,000 coordinates each were then analyzed for each gradient to obtain an equivalent number of estimates of $\mathrm{B}(x)$. The extents of the shaded area in Fig. 1C are obtained as the average $\mathrm{B}(x)$ plus/minus its standard deviation calculated over 10^6 $\mathrm{B}(x)$ bootstrapped profiles.

Derivation and identification of the mathematical model

Starting from a Fokker-Planck approximation of the motion of B. subtilis in an oxygen gradient (Supplementary Information) we derived the expression of V_C reported in Eq. 2 in the main text. In order to fully characterize the model we need to identify each of its three parameters K_1, K_2 and χ_0 - note that D_B is measured experimentally (see Supplementary Information and Fig. S2). To this aim we developed a genetic-algorithm-based multi-experimental fitting procedure designed to find the combination of parameter values that minimized the sum of the squared errors between model predictions and experimental data

$$\mathrm{SSE}(K_1, K_2, \chi_0) = \sum_{i=1}^{n} \frac{\sqrt{(B_E(x) - B_S(x))^2 \cdot w(x)}}{n} \tag{55}$$

where $n = 33$ is the number of experimental designs, $w(x)$ is a vector of weights increasing

linearly from 1 to 1000 (empirically found to ensure the best results in terms of prediction error were attained), $B_E(x)$ are the experimental data and $B_S(x)$ the simulated accumulation profiles via numerical integration ($\Delta x = 10$ nm) of:

$$B(x) = \frac{e^{\frac{\chi_0 \nabla C}{D_B} \int_0^x f(\xi) d\xi}}{\int_0^W f(\xi) d\xi} \tag{56}$$

with test channel width $W = 460\ \mu m$ and $f(\xi) = 1/((K1 + C(\xi))(K2 + C(\xi)))$ for the model in Eq. 2 in the main text. This expression of $\mathrm{B}(x)$ can be obtained plugging Eq. 2 in Eq. 1 in the main text, using the linearity of the oxygen gradient (i.e. ∇C independent of ξ) and posing $\frac{\partial B}{\partial t} = 0$. At each iteration the genetic algorithm generated a number of random solutions, ranked them based on Eq. 55, the worst solutions, selected the best ones and applied "cross-over" and "mutation" to obtain new solutions to be evaluated at the next iteration [50]. The search for a solution stopped when a stall was detected, i.e., when the average change in $\mathrm{SSE}(\chi_0, K_1, K_2)$ over 50 iterations was smaller than 10^{-6}. The reported parameter set is the best combination identified over 100 repetitions of this procedure. We adopted the same method to identify the parameter values for all models (see Supplementary Information).

Robustness analysis of parameter estimates

Although very powerful at solving complex optimization problems, Genetic Algorithms do not provide any guarantee of convergence. As a consequence of this, a set of "optimal parameters"

obtained as a result of the optimization, might actually be a local, rather than a global solution - these are solutions that optimize the objective function in a sufficiently large neighborhood of, but not the entire, space of parameters. Yet, at the end of the parameter optimization process we would ideally identify a set of values that minimizes the cost function (Eq. S62) globally rather than locally.

To assess whether the values obtained from the Genetic Algorithm could be outcompeted by other combinations of values, we decided to adopt a Naive Grid Search approach. The principle behind this method is simple: the set of values each parameter can take is discretized and all the combination of discretized parameters are evaluated using the cost function. The more fine-grained the discretization is, the more this approach resembles an exhaustive search. The main limitation of this approach is that for large numbers of parameters and/or parameter values the number of objective function evaluations quickly increases and ultimately makes the problem intractable.

As customary in these cases, we assigned to each parameter identification task (i.e., each model among the ones we considered) a budget of "function evaluations" equal to 10^5. For each of the i parameters in that model, we identified a physically feasible set of values, and discretized it into M values, with M being the closest integer to $10^{\frac{5}{i}}$. We then evaluated the cost function for each of these combinations and, for each model, the value of the minimum cost identified by the Naive Grid Search method was compared to the minimum found by the Genetic Algorithm (Fig. S10).

For both the KS and the LS models (1 and 2 parameters, respectively) we confirmed that the Naive Grid Search identified values of the optimal parameters substantially undistinguishable from the ones returned by the Genetic Algorithm. For the RTBL and the Finite Range Log-sensing regime,

instead, the Naive Grid Search algorithm returned values different from the Genetic Algorithm and, in both cases, characterized by higher value the cost function - suggesting that the parameter values identified by the Naive Grid Search are not global optima. These results indicate that it is unlikely that the parameter sets identified by the Genetic Algorithm for our model represent local optima and that they are instead the global optima we sought.

Model validation on transient aerotaxis

As a stringent validation of the model, we tested its performance in predicting the population migration in a transient aerotaxis experiment. At the start of the experiment, sink and source channels both contained a flow of 21% oxygen and cells were allowed time to equilibrate to their steady state distribution, which was uniform given the uniform oxygen concentration (Fig. 4). At time zero we started flowing 0% and 0.05% oxygen in the sink and source channels, respectively, and recorded the spatial distribution of bacteria across the test channel at 100 frames/s for 4 min To produce $\mathrm{B}(x)$, we binned 200 frames (2 s) in one time point, in order to minimize noise. The model prediction was obtained by integrating Eqs. 2 and 1 numerically with COMSOL (Comsol Inc., MA). We modeled oxygen dynamics using the diffusion equation and representing the microfluidic device as a one-dimensional domain with three parts: the 460 μm wide test channel (460 μm wide) and the two, 220 μm wide, flanking PDMS walls, at the outer end of which the experimentally imposed source and sink oxygen concentrations were prescribed. We note that, given the relative composition of the Cap Assay Minimal medium (essentially water supplemented with very small quantities of salts, amino acids and sorbitol) and, coherently with what has been previously reported[16], we

approximated the growth medium as water for the purpose of our simulations; therefore we set the diffusion coefficient of oxygen in water to $2 \cdot 10^{-9}$ m^2/s. We observe that: (a) temperature fluctuations have been ignored here as all the experiments have been carried out under temperature control, (b) the density of bacteria was low enough[10] (OD_{600}=0.03) to allow us to ignore the effect of respiration on the gradient and (c) although we do not expect inhomogeneity to be introduced in the PDMS matrix as part of the microfabrication process, we did not assess how any residual heterogeneities would have affected the diffusion dynamics. Oxygen profiles obtained as a result of the simulations were then used as input in the bacterial transport equation (Eqs. 1 and 2), which was solved in the test channel with a time step of 0.1 s and a spatial resolution of 4.6 μm, after ensuring these choices were sufficient to have a converged solution. The models used in our comparative analysis are introduced and discussed in this section.

KS model

Developed in the early 70s by Keller and Segel [41], this was the first mathematical model that aimed at quantitatively capturing chemotaxis. Studying slime molds the authors observed that chemotaxis is the result of random (diffusion) and directed motility (advection) of microorganisms and consequently decided to use advection-diffusion models to capture it. When it came to the choice of an expression for the advection (i.e. chemotactic) speed, V_C, Keller and Segel took a phenomenological approach and assumed it was directly proportional to the chemoattractant gradient ∇C (rescaled by a constant χ_0) and inversely proportional to C the chemoattractant concentration:

$$V_C = \chi_0 \frac{\nabla C}{C}$$

This expression of V_C has a singularity for $C = 0$ M, i.e. bacteria achieve higher and higher chemotactic speed as the concentration of the chemoattractant decreases; a rather counterintuitive result. However, in a follow-up paper [44], Keller and Segel noted this specific choice of the functional form of V_C allowed their model to predict band-formation: a phenomenon observed few years back in *in-vivo* experiments carried out by Adler [45]. A preliminary confirmation of the validity of this model came few years later when Holz and Chen [46] demonstrated it was able to predict *E. coli*'s response to serine gradients.

Interestingly, even before Dahlquist and co-workers first suggested bacteria responded to relative, rather than absolute, changes in chemical concentrations [47], the KS model supported logarithmic sensing at all concentrations ($V_C \propto \nabla C/C \; \forall C$). Recent studies highlighted that logarithmic sensing, and therefore gradient rescaling, only takes place over a finite interval of concentrations [48], pointing at a fundamental limitation of the KS model.

The need to provide biological ground to the proposed models then emerged and triggered a quest for a more "biologically realistic" alternative [40] to the original KS model; this is the direction Lapidus and Schiller took while developing their model (LS) [51].

To test the ability of this model to recapitulate our experimental results, and compare its prediction capabilities with other models, we adopted the same approach reported in the main text for the

"finite-regime log-sensing" model we propose (see "Derivation and Identification of the Mathematical Model"). We ran 100 instances of a genetic algorithm meant to identify the value of χ_0 (the only free parameter in this model) that minimizes the average mismatch between model prediction and experimental results over the whole dataset. It should be noted that, based on Eq. (4) (see main text) and assuming D_B does not depend on space, the steady state distribution of bacteria $B(x)$ can be rewritten as:

$$B(x) = \frac{e^{\frac{\chi_0 \nabla C}{D_B} \cdot \int_0^x \frac{1}{C(\xi)} d\xi}}{\int_0^W \frac{1}{C(\xi)} d\xi} \tag{57}$$

where we observe that χ_0 and D_B in this model are "structurally unidentifiable". Given the physical meaning of the χ_0 and D_B we imposed a non negativity constraint on the optimization problem meant to identify the value of χ_0/D_B, collected the results of the optimization procedures and plotted the prediction of the model achieving the best accuracy ($\chi_0/D_B = 2.66\ \mu m$, Fig. S3).

LS model

Motivated by the mismatch between model predictions of the original KS formulation [52–54] and the experiments reported in [47], Lapidus and Schiller set out to propose a functional form of the chemotactic speed that incorporated one of the most relevant biochemical properties of chemoreceptors: the dissociation constant between the ligand and the receptor itself.

They succeeded in this effort and proposed a formulation of V_C directly proportional to the chemo-

tactic sensitivity coefficient χ_0 and inversely proportional to the squared sum of K and the chemoattractant concentration C:

$$V_C = \chi_0 \frac{\nabla C}{(K + C)^2}$$

By using population scale measurements of bacterial fluxes, not only were Lapidus and Schilller able to identify the values of χ_0 and K, they also showed the predictions of their model were in good agreement with the experimental results.

It is worth noting that, while achieving good performance in capturing the experimental results in [51], the LS model does not support logarithmic sensing. Moreover, as our understanding of the cascade of signaling events leading to chemotaxis furthered, an increasing number of approaches focused on bridging single cell behavior and population level phenomena.

To assess the ability of this model to capture our data we followed the same approach described for the KS model. In this case, however, the parameters to be identified are both χ_0/D_B and K. We set non-negativity constraints for this identification task following the same line of reasoning mentioned above and recorded the results of the 100 optimization procedures. The solutions to the optimization problem is plotted in Fig. S4 ($\chi_0/D_B = 57.89$ and $K = 1.39 \cdot 10^{-5}$ M).

RTBL model

The RTBL model, developed by Rivero and colleagues [43], achieves a macroscopic characterization of bacterial chemotaxis using microscopic variables involved in the chemotactic response of single cells (e.g. receptor occupation and swimming speed). In order to derive their model Rivero and colleagues considered two sub-populations of bacteria (p^+ and p^-) exposed to a chemoattractant gradient in a 1D domain. Each bacterium can either proceed from left to right or viceversa; this will determine which subpopulation it belongs to. Tumbling makes a bacterium switch from one group to the other; just like we would expect to happen *in-vivo*, the probability of tumbling depends on the time derivative of the number of bound receptors. In this framework, following the steps reported in Appendix A in [55], one can derive the expression of the chemotactic speed V_C:

$$V_C = \frac{2}{3} V \tanh\left(\frac{\chi_0}{2V} \frac{\nabla C}{(K+C)^2}\right)$$

where V is the swimming speed of bacteria.

While being one of the most advanced results in chemotaxis, this model does not recapitulate the most recent observations [56] regarding logarithmic sensing and Fold Change Detection in *E. coli*'s chemotaxis.

Consistently with what we previously reported, we probed the ability of the RTBL model to capture our dataset running 100 instances of our optimization procedure. In this case the parameters to be identified were three: χ_0, K and V. For all of them we set non-negativity constraints, following

the considerations we previously discussed; moreover we restricted V, the swimming speed, to not exceed 40 $\mu m/s$ (we set this constraint according to experimental quantification of bacterial swimming speed we obtained while measuring D_B). Also in this case we collected statistics on the prediction error of the solutions identified during the 100 runs of the optimization procedure (Fig. 5) and we plotted the results from the simulation of the best among the 100 solutions identified by the genetic algorithm in Fig. S5 ($\chi_0 = 7.10 \cdot 10^{-8}$ m^2/s, $K = 7.01 \cdot 10^{-6}$ M and $V = 39.4 \cdot 10^{-5}$ m/s).

References

33. J.R. Howse,R.A.L. Jones, A.J. Ryan,T. Gough, R. Vafabakhsh, and R. Golestanian, *Self-Motile Colloidal Particles: From Directed Propulsion to Random Walk* Physical Review Letters, 99. doi:10.1103/PhysRevLett.99.048102 (2007).

34. A. Sokolov, and I.S. Aranson,*Physical properties of collective motion in suspensions of bacteria* Physical Review Letters, 109. doi:10.1103/PhysRevLett.109.248109 (2012).

35. D.S. Bischoff, and G.W. Ordal *Bacillus subtilis chemotaxis: a deviation from the Escherichia coli paradigm*. Molecular Microbiology, 6(1), 2328. doi:10.1111/j.1365-2958.1992.tb00833.x

36. Othmer H. G., Dunbar S. R., and Alt W. Models of dispersal in biological systems. *J Math Biol*, 26(3):263–98, 1988.

37. L. Jiang, Q. Ouyang, and Y. Tu. Quantitative modeling of escherichia coli chemotactic quantitative modeling of escherichia coli chemotactic motion in environments varying in space and

time. *PLoS Computational Biology*, 6(4):e1000735, 2010.

38. J. Monod, J. Wyman, and J. P. Changeux. On the nature of allosteric transitions: a plausible model. *J. Mol. Biol.*, 12:88–118, May 1965.

39. Y. Tu, T. S. Shimizu, and H. C. Berg. Modeling the chemotactic response of Escherichia coli to time-varying stimuli. *Proc. Natl. Acad. Sci. U.S.A.*, 105:14855–14860, 2008.

40. M. Tindall, P. Maini,S. Porter, and J. Armitage *Overview of mathematical approaches used to model bacterial chemotaxis II: bacterial populations*, Bulletin of Mathematical Biology, 70(6), 15701607 (2008).

41. E. Keller, and L. Segel *Model for chemotaxis*, J. Theor. Biol. 30(2), 225234 (1971).

42. M.A. Rivero-Hudec, and D. Lauffenburger *Quantification of bacterial chemotaxis by measurement of model parameters using the capillary assay* Biotech. Bioeng. 28, 11781190 (1986).

43. M.A. Rivero, R.T. Tranquillo, H.M. Buettner, and D.A. Lauffenburger *Transport models for chemotactic cell-populations based on individual cell behavior* Chem. Eng. Sci. 44:28812897 (1989).

44. E. Keller,and L. Segel, *Traveling bands of chemotactic bacteria: a theoretical analysis* Journal of Theoretical Biology. 30(2), 235248 (1971).

45. J. Adler, *Chemotaxis in bacteria* Science 153, 708716 (1966).

46. M. Holz, and S.H. Chen, *Spatio-temporal structure of migrating chemotactic band of Escherichia coli. I. Traveling band profile* Biophysical Journal, 26, 243261 (1979).

47. F.W. Dahlquist, P. Lovely and D.E. Koshland *Quantitative analysis of bacterial migration in chemotaxis* Nat. New Biol. 1972;236:120123 (1972).

48. Y.V. Kalinin, L. Jiang, Y. Tu, and M. Wu, *Logarithmic sensing in Escherichia coli bacterial chemotaxis*, Biophys. J. 96, 24392448 (2009).

49. T. Scribner,L. Segel and E. Rogers, *A numerical study of the formation and propagation of travelling bands of chemotactic bacteria* J. Theor. Biol. 46, 189219 (1974).

50. Z. Michalewicz,*Genetic Algorithms, Numerical Optimization, and Constraints* Proc. sixth Int. Conf. Genet. algorithms 195, 151158 (1995).

51. R. Lapidus and R. Schiller, *Model for the chemotactic response of a bacterial population* Biophys. J. 16, 779789 (1976).

52. Nossal, R.,Weis, G., 1973. Analysis of a densitometry assay for bacterial chemotaxis. J. Theor. Biol. 41(1), 143147.

53. Segel, L., Jackson, L., 1973. Theoretical analysis of chemotactic movements in bacteria. J. Mechanochem. Cell Motility 2, 2534.

54. Lapidus, R., Schiller, R., 1974. A mathematical model for bacterial chemotaxis. Biophys. J. 14, 825834.

55. Ahmed, T., and Stocker, R. (2008). Experimental verification of the behavioral foundation of bacterial transport parameters using microfluidics. Biophysical Journal, 95, 44814493.

56. Lazova, M. D., Ahmed, T., Bellomo, D., Stocker, R., and Shimizu, T. S. (2011). Response rescaling in bacterial chemotaxis. Proceedings of the National Academy of Sciences of the United States of America, 108, 1387013875.

57. Aminzare, Z., and Sontag, E.D. (2013). Remarks on a population-level model of chemotaxis: advection-diffusion approximation and simulations. arXiv:1302.2605v1.

Table 1: **Oxygen concentrations inside the test channel**. For each oxygen mixture flown in in the sink and source the actual concentrations within the test channel, as well as the number of replicates, are reported here. In each case the bacteria were exposed to a linear gradient with minimum C(0 μm) and maximum C(460 μm).

Sink [%]	**Source [%]**	**C**(0 μm) **[M]**	**C**(460 μm) **[M]**	**Replicates**
0	0.01	6.04E-09	1.24E-07	3
0	0.025	1.51E-08	3.10E-07	2
0	0.05	3.02E-08	6.20E-07	7
0	0.075	4.53E-08	9.30E-07	2
0	0.1	6.04E-08	1.24E-06	7
0	0.25	1.51E-07	3.10E-06	4
0	0.5	3.02E-07	6.20E-06	4
0	1	6.04E-07	1.24E-05	5
0	2.5	1.51E-06	3.10E-05	2
0	5	3.02E-06	6.20E-05	4
0	10	6.04E-06	1.24E-04	2
0	20	1.21E-05	2.48E-04	2
0	30	1.81E-05	3.72E-04	2
0	40	2.41E-05	4.96E-04	3
0	50	3.02E-05	6.20E-04	3
0	60	3.62E-05	7.44E-04	2
0	70	4.23E-05	8.68E-04	2
0	80	4.83E-05	9.92E-04	2
0	90	5.43E-05	1.12E-03	3
0	100	6.04E-05	1.24E-03	2
5	10	6.80E-05	1.27E-04	2
5	15	7.10E-05	1.89E-04	3
10	10	1.30E-04	1.30E-04	2
10	15	1.33E-04	1.92E-04	2
10	30	1.42E-04	3.78E-04	2
10	50	1.54E-04	6.26E-04	2
10	70	1.66E-04	8.74E-04	2
10	90	1.78E-04	1.12E-03	2
15	20	1.98E-04	2.57E-04	2
20	20	2.60E-04	2.60E-04	2
20	40	2.72E-04	5.08E-04	2
20	60	2.84E-04	7.56E-04	2
20	80	2.96E-04	1.00E-03	2
30	30	3.90E-04	3.90E-04	2
30	50	4.02E-04	6.38E-04	2
30	70	4.14E-04	8.86E-04	2
40	40	5.20E-04	5.20E-04	2
50	50	6.50E-04	6.50E-04	2
60	60	7.80E-04	7.80E-04	2
70	70	9.10E-04	9.10E-04	2
80	80	1.04E-03	1.04E-03	2
90	90	1.17E-03	1.17E-03	2
100	100	1.30E-03	1.30E-03	2

Supplementary Figures

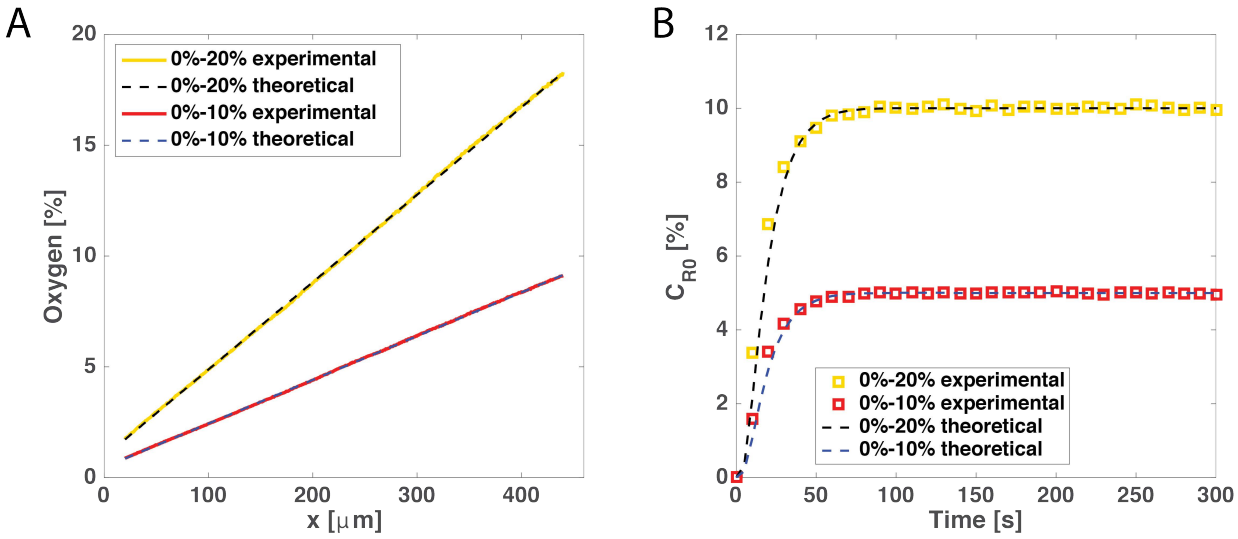

Figure 1: **In-silico and in-vitro analysis of oxygen diffusion in the microfluidic device**. In panel A the steady state oxygen concentration is plotted as a function of space for both the gradients 0%-20% and 0%-10%. Dashed and solid lines represent, respectively, model predictions and experimental quantifications. In panel B C_{R0}, the rescaled oxygen concentration at mid-channel is plotted against time: dashed line is model prediction, squares are experimental measurements.

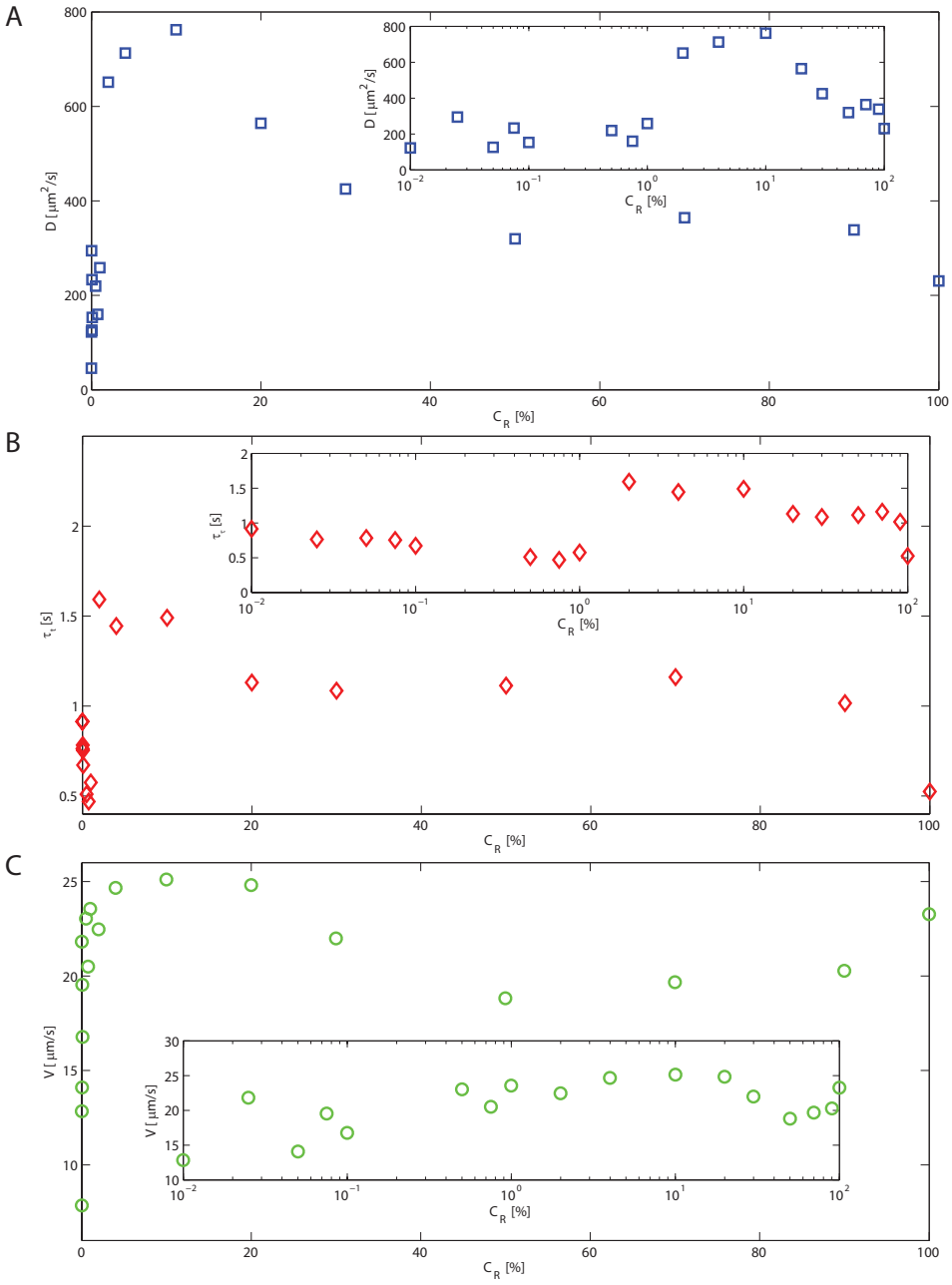

Figure 2: **Quantification of** D_B. (A) shows the bacterial diffusion coefficient, D_B, plotted against oxygen concentration. (B) and (C) show how the two physical quantities, swimming speed V (measured) and tumble time τ_t (fitted), contribute to shape D_B (Eq. S1) and their dependence on O_2. Semilog plots (inset) illustrate the dependence of these quantities at low oxygen concentrations

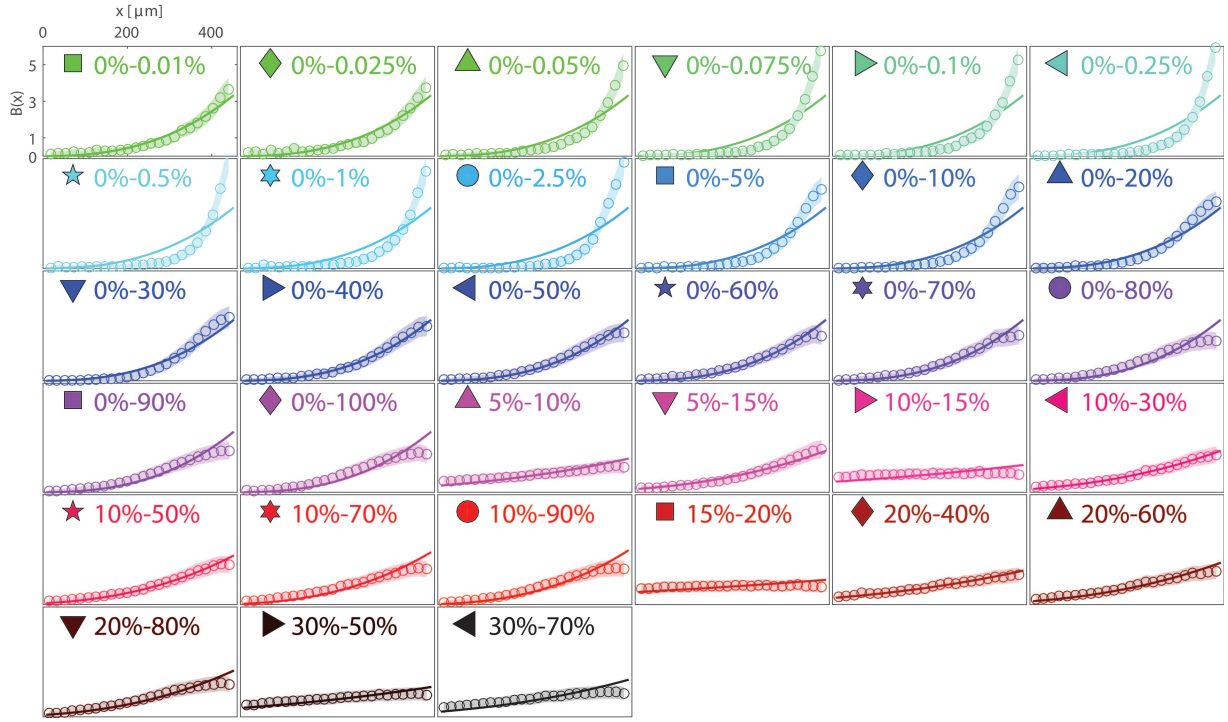

Figure 3: **Best KS model predictions**. Numerical simulation (solid lines) of the KS model with the value of χ_0/D that minimizes the weighted SSE. Experimental data are represented with circles, shaded area around the them represent $\pm$ standard deviation on the estimates of B(x).

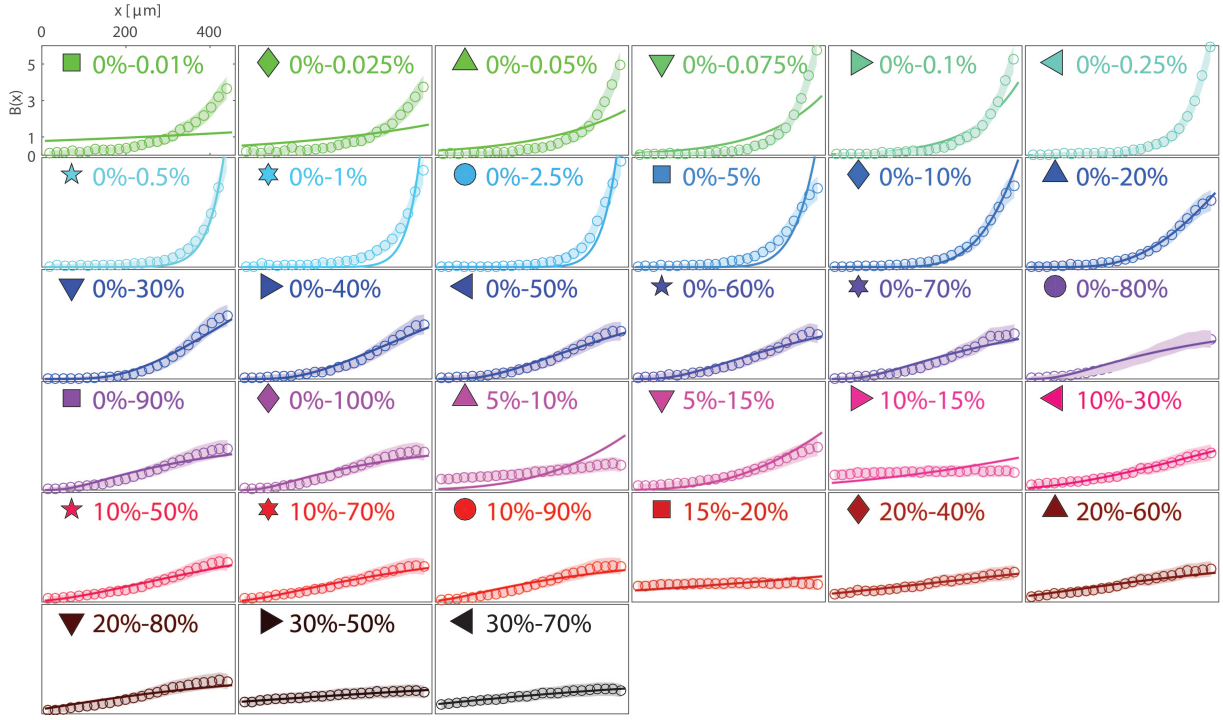

Figure 4: **Best LS model predictions**. Numerical simulation of the RL model with the values of χ_0/D and K that minimize the weighted SSE. Data are presented as in Fig. S3.

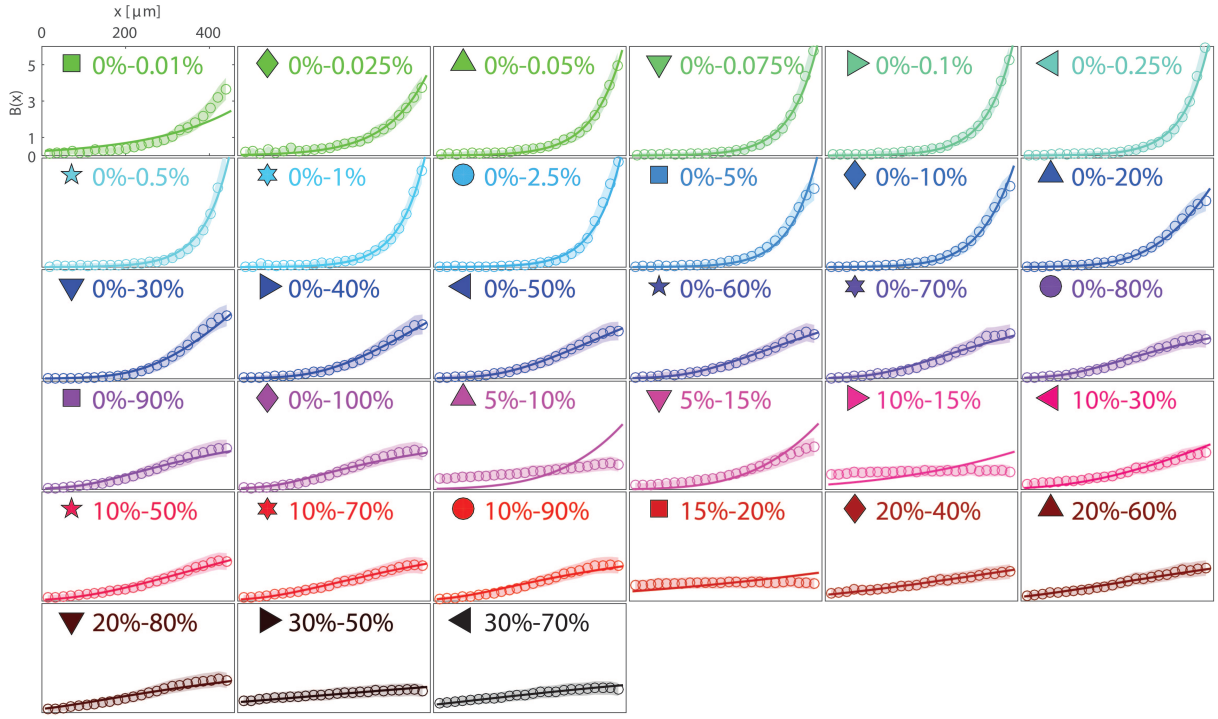

Figure 5: **Best RTBL model predictions**. Numerical simulation of the RTBL model with the values of v, K and χ_0 that minimize the weighted SSE. Data are presented as in Fig. S3.

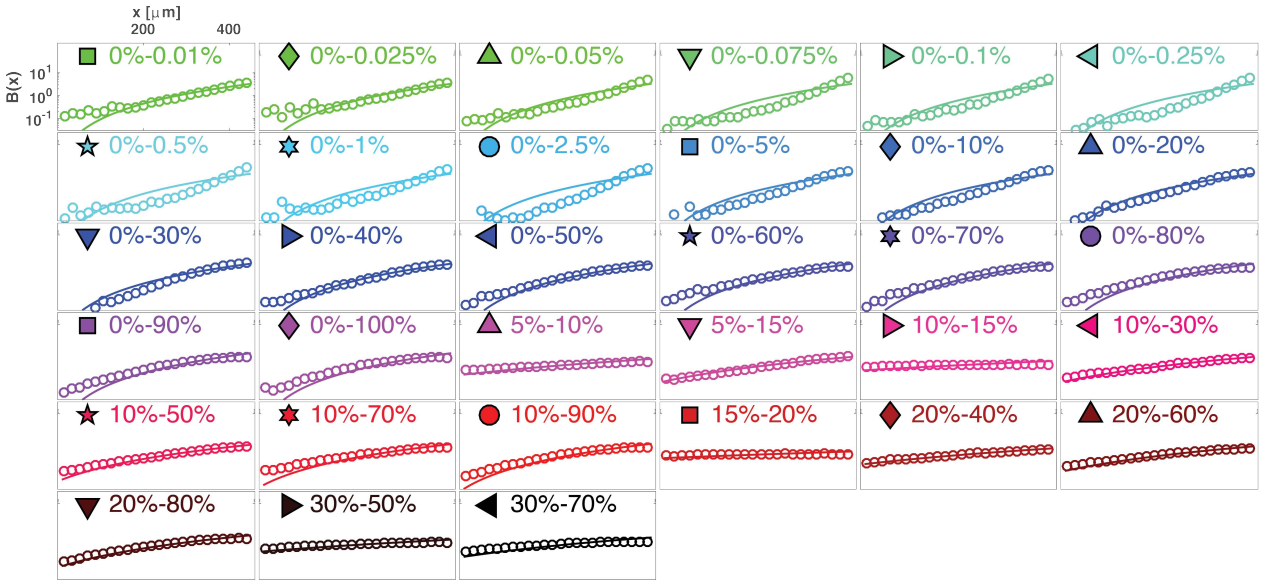

Figure 6: **Best KS model predictions - x axis in log-scale**. The same data presented in Fig. S3 is here presented in log-scale (x axis).

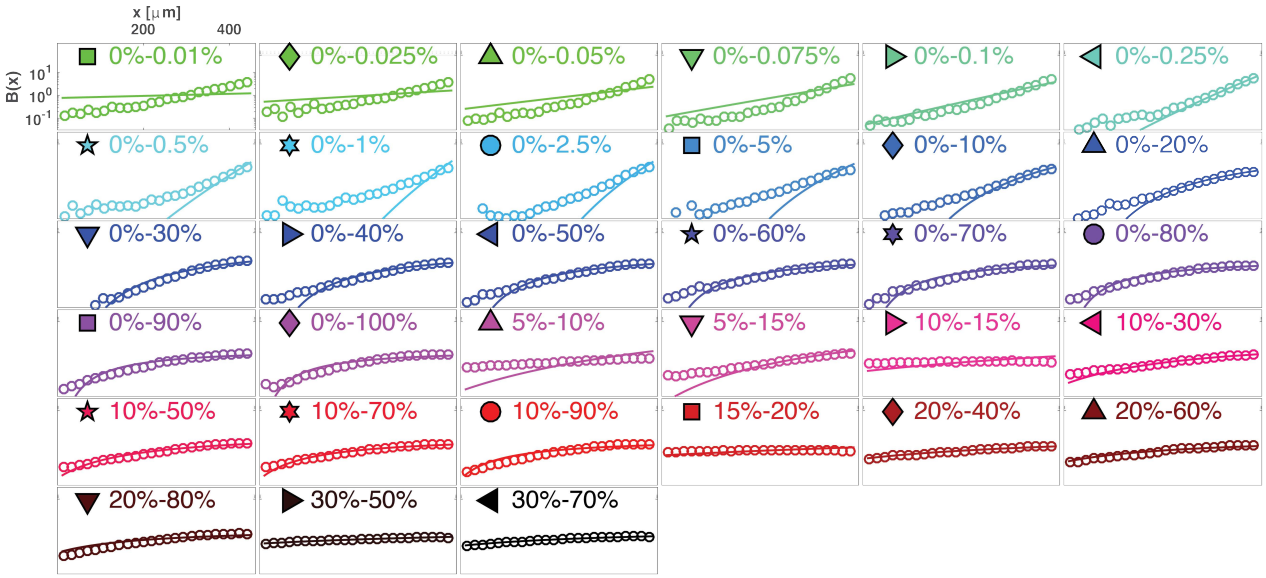

Figure 7: **Best LS model predictions - x axis in log-scale**. The same data presented in Fig. S4 is here presented in log-scale (x axis).

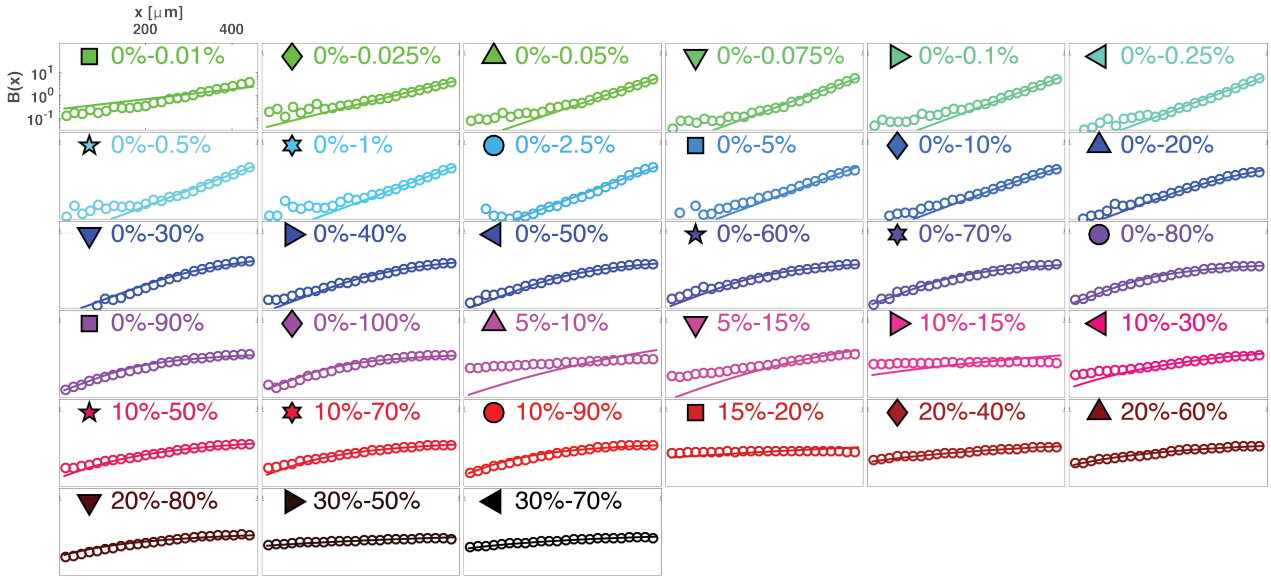

Figure 8: **Best RTBL model predictions - x axis in log-scale**. The same data presented in Fig. S5 is here presented in log-scale (x axis).

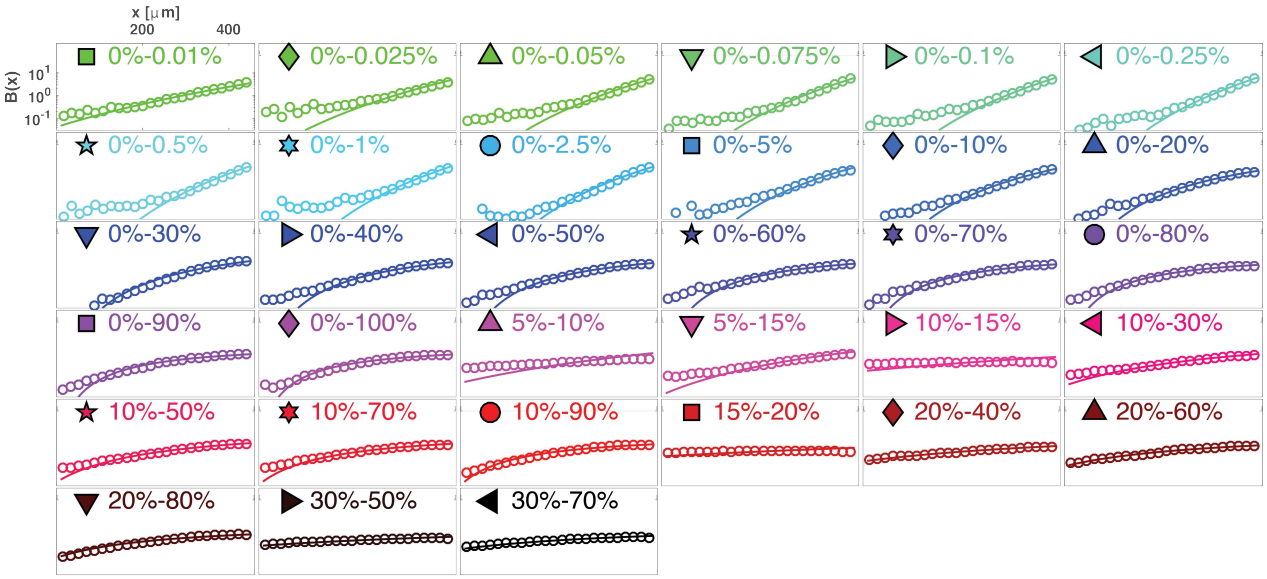

Figure 9: **Best model predictions for the Finite regime log-sensing model - x axis in log-scale**.

The same data presented in Fig. 1 is here presented in log-scale (x axis).

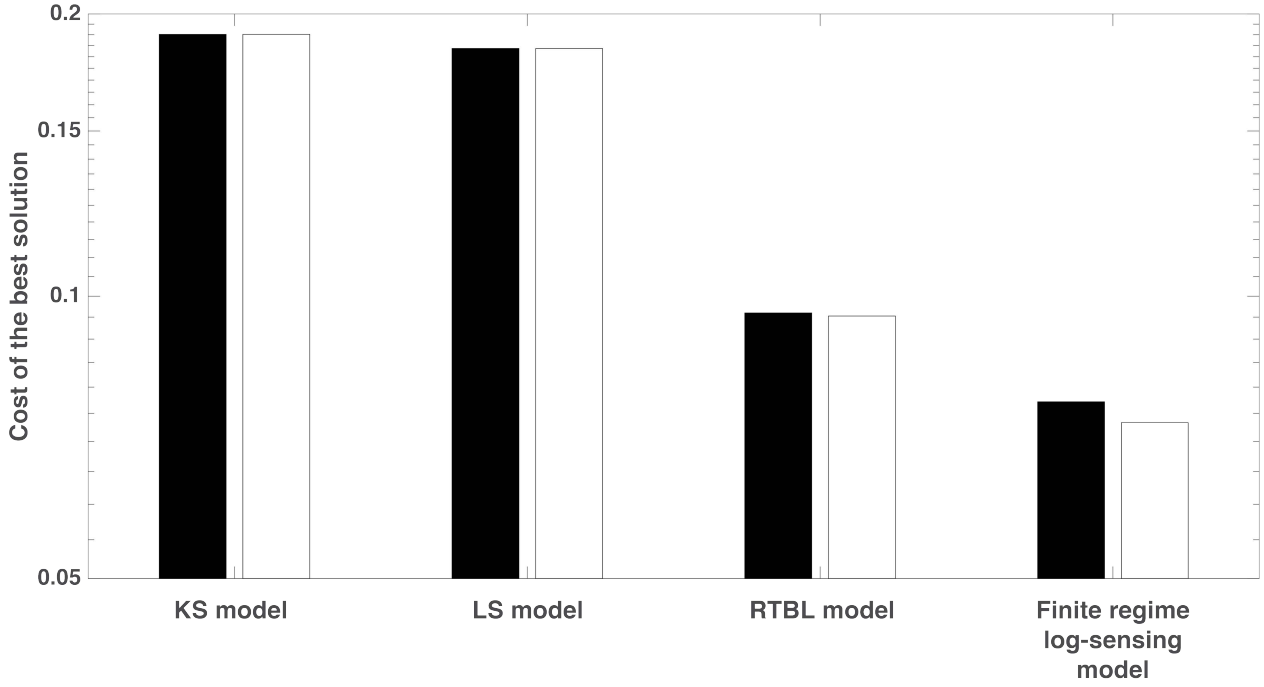

Figure 10: **Comparison of Naive Grid Search and Genetic Algorithm parameter optimization**. The minimum value of the cost function is here plotted for each of the four models as identified by the Naive Grid Search (black bars) and the Genetic Algorithm (white bars). In all the cases the Genetic Algorithm was able to identify a solution that matched or exceeded the quality of the solution identified as best by the Naive Grid Search.

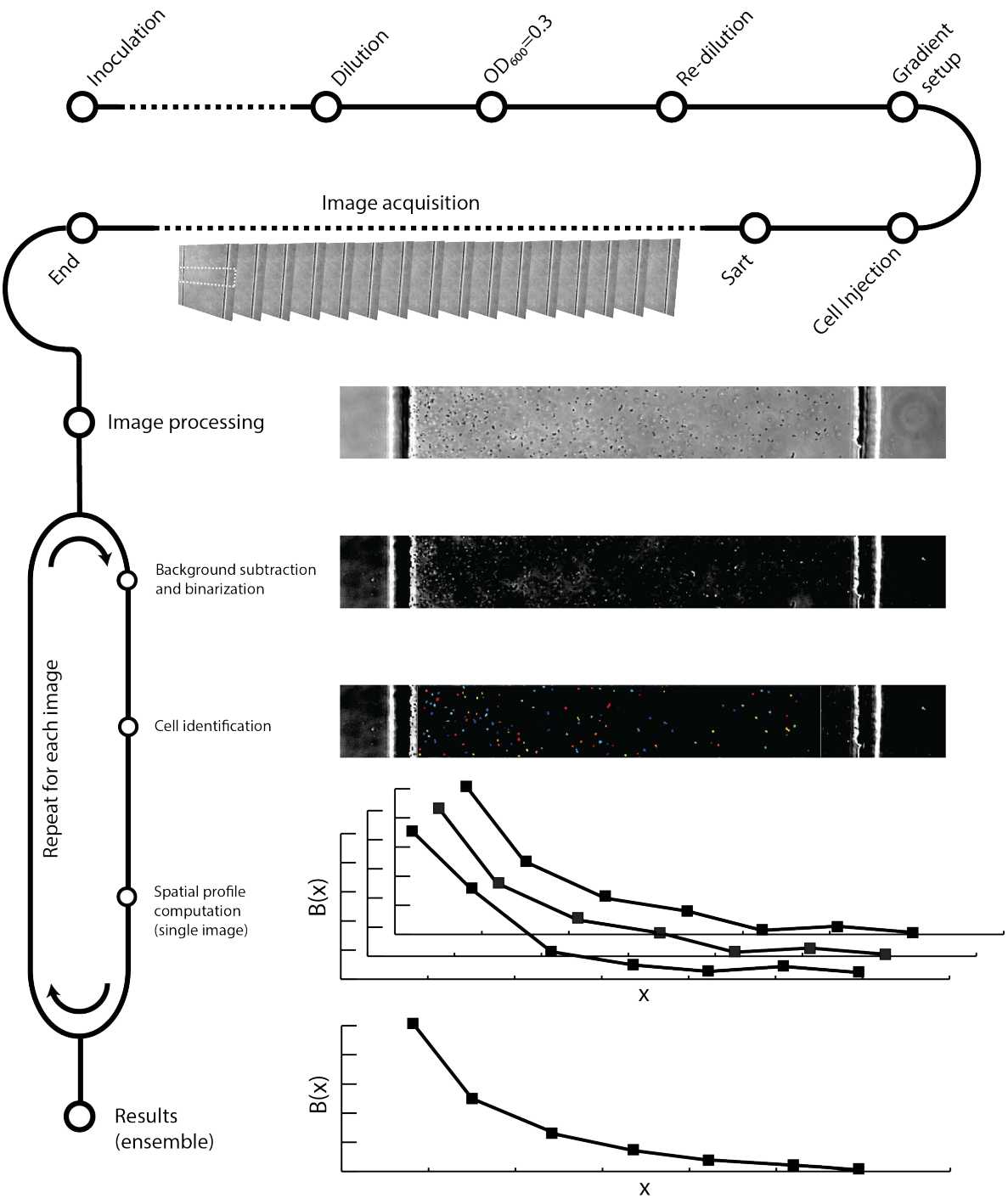

Figure 11: **Experimental setup**. From culturing cells (”Inoculation” to ”Redilution”) to acquiring the microscopy images (“Image acquisition”) and analysing them to extract B(x) for each frame (“Spatial profile computation”), then pooled to compute the final B(x) (“Results”), the sequence of steps of a typical experiment of the type presented in Figure 1C is presented here.

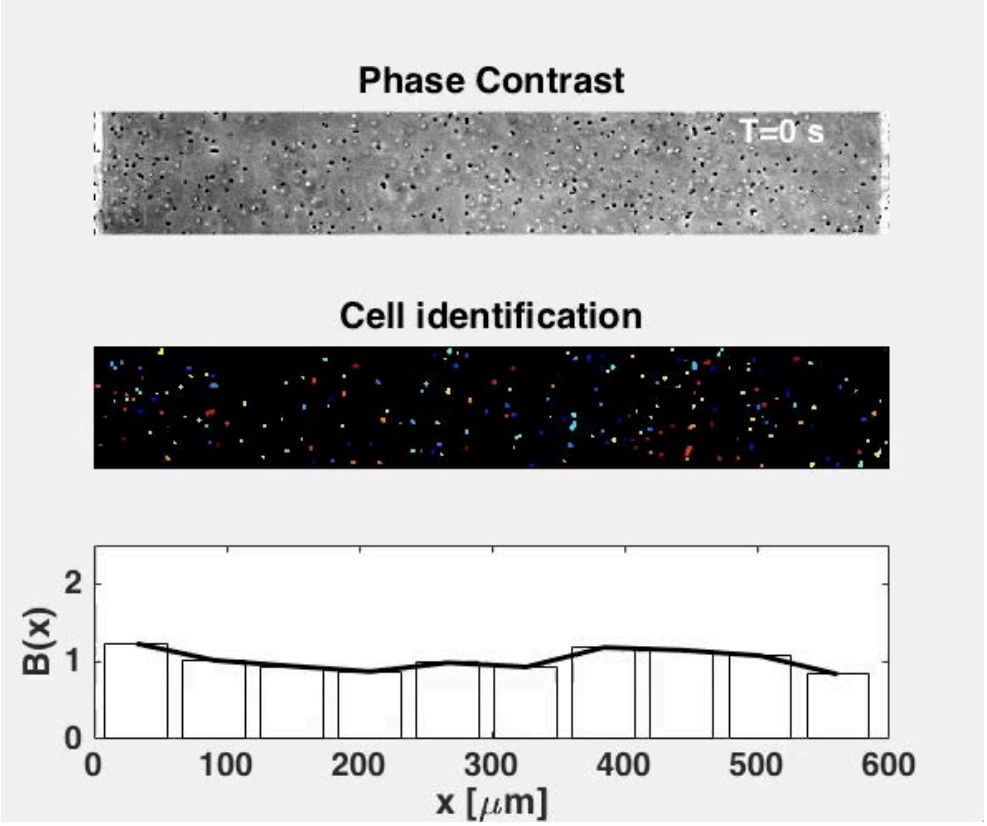

Video S1: **Dynamics of bacteria accumulation**. An example of the dynamics of bacteria accumulation is reported in this video. At time t=0 s the gradient is switched from 20%-20% to 0%-100%; images are acquired at 1 fps in this experiment. Bacteria (black in "Phase contrast"), each identified with a different colour by the image processing processing algorithm ("Cell Identification"), start migrating towards the oxygen rich end (left) until a steady state distribution is reached. In this experiment a concentration of bacteria $\sim$ 3 times higher than usual has been used (to limit the impact of noise, still present, on the computational of the B(x) for each frame, lower panel) as well as a wider test channel (600 μm in width).